J. Fluid Mech. (1989), *vol.* 204, *pp.* 263–293
Printed in Great Britain

Observations of a nonlinear solitary wave packet in the Kelvin wake of a ship

By ELLEN D. BROWN[1], STEVEN B. BUCHSBAUM[1,2], ROBERT E. HALL[1], JOHN P. PENHUNE[1], KURT F. SCHMITT[1], KENNETH M. WATSON[2] AND DONALD C. WYATT[1,3]

[1] Science Applications International Corporation, San Diego, CA 92121, USA

[2] Scripps Institution of Oceanography, San Diego, CA 92093, USA

[3] Department of Applied Mechanics and Engineering Sciences, University of California, San Diego, CA 92093, USA

(Received 15 June 1988 and in revised form 27 December 1988)

Thirty data sets of wavestaff measurements of a solitary feature in the Kelvin wake of the Coast Guard cutter *Point Brower* are analysed. The average characteristics of the feature between 1 and 4 km aft of the ship are shown to be consistent with those of an oblique nonlinear solitary wave packet. The ship speed is 7.7 m/s (Froude number 0.49) and the waves that comprise the packet have an average frequency of 3.28 rad/s. The ship speed and the wave frequency, together with Kelvin wake kinematics, imply that the feature appears at an average wake half-angle of 10.9°. The packet does not exhibit linear dispersion beyond 1 km aft of the ship and its average width is 8.9 m (measured at e^{-1} of the peak variance). The average amplitude is 1.1 times the theoretical amplitude of an oblique nonlinear solitary wave packet with the observed width. There is considerable variability from run to run, and there is evidence of dispersive spreading before 1 km aft of the ship. An aerial photograph shows a sinuous fluctuation of the feature; possible explanations for the fluctuation include small variations in initial conditions or a sinuous instability. The solitary feature is a possible explanation for the long bright lines observed in SEASAT SAR images in light to moderate winds and observed in sun glitter photos taken from the space shuttle.

1. Introduction

Kelvin's classical research on the linear surface wave wake of a ship was completed a century ago (Kelvin 1887; see also Stoker 1957). In this work, Kelvin demonstrated that the wake consisted of a transverse wave field that propagated in the direction of motion of the ship, a diverging wave field that propagated roughly perpendicular to this direction, and a 19.5° cusp line that served as the outer boundary of both fields. Since Kelvin's time, there has been considerable progress throughout the field of hydrodynamics. Most of the research in the field of ship hydrodynamics, however, has focused on the flow near the ship, because that region is important to ship performance. The far-field wake, which was the subject of Kelvin's research, has received less attention. This situation changed in 1978 when the synthetic aperture radar (SAR) on the SEASAT satellite returned a number of images of surface ships and their wakes (Fu & Holt 1982). Although some features in the classical Kelvin wake were occasionally observed in light winds (the cusp line and the transverse wave field), there were a number of wake images with isolated bright lines that

appeared at angles less than 19.5° and that extended up to several kilometres aft of the ship (Hammond, Buntzen & Floren 1985). Although some structure is typical in the diverging wave field, thin isolated lines with the length and intensity of the features that appeared in the SAR images were not expected. These new features stimulated research on the far-field wake of a surface ship.

In calm wind conditions, the SEASAT lines took the form of bright narrow-V features. In 1983, the narrow-V features were examined during the Georgia Strait Experiment. It was determined that the features were due to Bragg scattering from decimetre-scale, time-dependent surface waves generated by wave breaking and turbulence near the ship (Munk, Scully-Power & Zachariasen 1987; see also Wyatt & Hall 1988, and Hall, Loeser & Wyatt 1987). In light to moderate wind conditions, some SEASAT lines appeared at wider angles (still less than 19.5°) and they were apparently due to a different physical mechanism. In this paper we present observations of an inner-angle feature in the wake of the Coast Guard cutter *Point Brower*. We show that the feature does not exhibit linear dispersion between 1 and 4 km aft of the ship and the average characteristics are consistent with those of an oblique nonlinear solitary wave packet. This offers a possible explanation for the long SEASAT lines in light to moderate winds.

Our experiment was motivated by observations made by two of us (J.P. & K.W.) of solitary features in the late wakes of ships. Aerial surveys were made by one of us (K.S.) to find an appropriate ship for the experiment. At the suggestion of K. Victoria (SAIC), the *Point Brower* was surveyed and a solitary feature was observed in the wake. The experiment consisted of measurements of sea surface height in the wake using an array of wavestaffs mounted on the ONR oceanographic tower, a fixed platform formerly located one mile off the San Diego coast. The experimental observations were compared to theoretical solutions for nonlinear solitary wave packets and linear dispersive Gaussian wave packets, as described herein.

The theory of Kelvin wakes, nonlinear solitary wave packets, and linear dispersive Gaussian wave packets is covered in §2. The experimental procedures are described in §3. In §4, we analyse the data and compare theory and experiment. Finally, in §5 we summarize the results.

The original goal of the data analysis was to determine whether the observed feature was linear or nonlinear and, if it was nonlinear, whether or not the characteristics were consistent with those of an oblique nonlinear wave packet. Accordingly, we have focused on the general evolution of the feature with distance aft and its average properties. However, as discussed in §4.2, our analysis has revealed considerable variability in the feature. We expect that this variability will motivate additional theoretical research, which may warrant a future re-examination of the data.

In our research we would have liked to have made a detailed comparison between the profile of the observed feature and the theoretical sech profile of an oblique nonlinear solitary wave packet. Unforunately, the observed profile was distorted by ambient waves, thereby limiting the comparison to gross properties, such as width and amplitude. We would also have liked to have examined the small nonlinear changes in certain kinematics of the feature, such as frequency, phase speed, and group velocity. However, the presence of ambient waves, the variability in the data, and the absence of a detailed aerial survey during the experiment prevented us from doing this. The nonlinear property that we have focused on is the general evolution of the width of the feature with distance aft.

2. Theoretical considerations

2.1. *Kelvin wake*

Linear Kelvin wake theory predicts a pattern of transverse and diverging waves generated by a moving pressure source (Kelvin 1887; see also Stoker 1957). These waves are confined within a wedge having a 19.5° half-angle. The predicted wave height has a local maximum near the cusp line at the outer edge. In the wake of a ship, however, wave steepness is determined by the detail of the hull form, and rays can appear within the diverging wave field. The simplest explanation for these rays is an interference pattern formed by the superposition of the wave fields generated at the bow and the stern. However, rays can also form within each of these wave fields owing to the finite size of the source regions at the bow and the stern. A hierarchy of approaches is used to model the wake produced by a specific hull (see the review articles by Wehausen 1973; von Kerczek 1975; Chapman 1977; and Yeung 1982; and the collection of articles in Webster 1986). Scragg (1983) used a numerical model and slender-ship theory to predict the wave field from panelized ship hull forms. It was found, for example, that steeply sloped, short-scale waves are generated by hull forms with a flared bow angle. The rays in a linear Kelvin wave field spread and decrease in amplitude owing to linear dispersion. If nonlinearity is significant and the rays evolve into nonlinear solitary wave packets, or if nonlinear solitary features are generated directly by the ship, then linear dispersion may be arrested.

No realistic nonlinear models have, to our knowledge, been developed to calculate the entire Kelvin wave field of a ship, although a considerable amount of research has been conducted on certain aspects of the problem (see the review articles listed above). For example, West *et al.* (1987) and Dommermuth & Yue (1988) used a nonlinear hydrodynamic theory to calculate the Kelvin wake of a moving pressure pulse. Hogben (1972) also examined some nonlinear wake effects. However, the limited range of scales in their models did not permit a detailed study of the inner wake features.

Observations of steeply peaked and long-lived wave packets in the Kelvin wakes of ships have led to conjectures that soliton-like features can be generated by a ship. The existence of theoretical solutions for oblique nonlinear solitary wave packets (see §2.2) has supported these conjectures because, within the Kelvin wake, the wave propagation angle is oblique to the wake ray angle. Akylas (1987) has shown that a steady oblique soliton does not form on the 19.5° cusp line because the component of the group velocity normal to the line is locally uniform with respect to changes in the component of the wavenumber normal to the line, thereby inhibiting steepening due to nonlinearly induced wavenumber variations. However, inside the cusp line, there is no such limitation in the diverging wave field.

The geometry for the ship's wake and the experiment is shown in figure 1. The ship travels at a speed U along the x' axis. The solitary feature appears at a wake half-angle α with respect to the ship's track. As discussed at the end of §2.2, the kinematics of the carrier wave in a nonlinear feature differ slightly from those in a linear feature. For now, we quote the linear results. Linear Kelvin theory predicts that the ship waves will be stationary with respect to the ship, thus the wavenumber will satisfy

$$k = \frac{g}{U^2 \cos^2 \theta}, \tag{1}$$

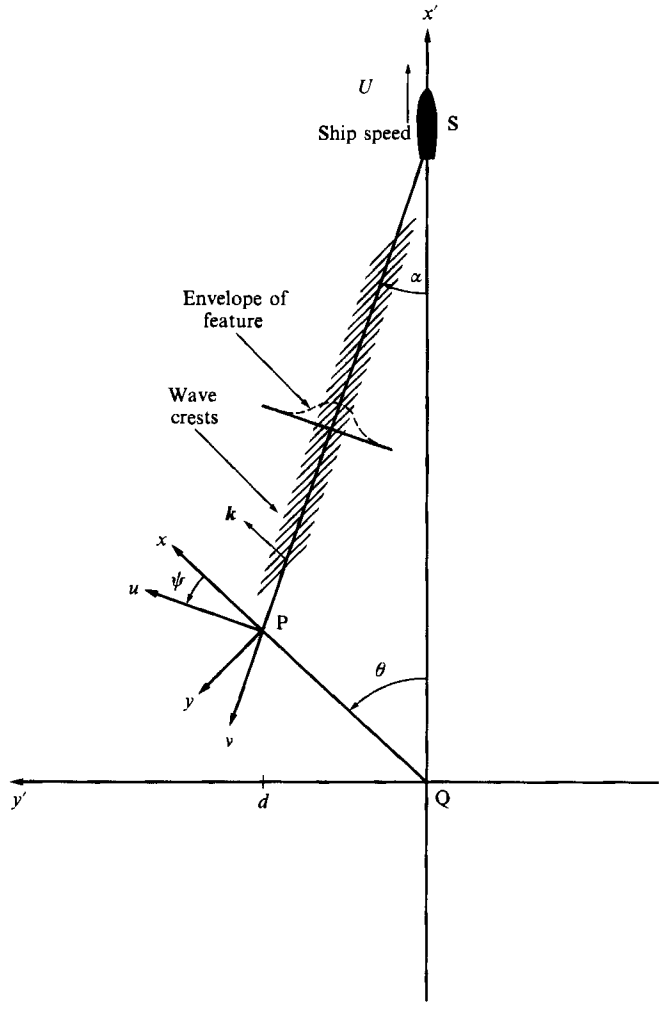

FIGURE 1. Schematic of the ship wake geometry. The ship is moving at speed U along the x' axis relative to all of the coordinate systems which are all ground-fixed. The figure shows the position of the solitary feature when it is observed by the wavestaff array which is located at P. The solitary feature appears at half-angle α with respect to the ship track. The carrier waves in the feature propagate with wavevector $\boldsymbol{k}$ parallel to the x-axis at an angle θ from the x' axis. The feature envelope propagates in a direction parallel to the u-axis at an angle ψ from the x-axis. The wavestaff array at P is at an offset distance d from the x' axis.

where $g = 9.8\ \mathrm{m/s^2}$ is the acceleration due to gravity and θ is the propagation angle of the wave number $\boldsymbol{k}$ with respect to the x' axis. The relation between α and θ, determined by the requirement that the waves propagate with the linear wave group velocity, is given by

$$\tan\theta = \frac{[1 \pm (1 - 8\tan^2\alpha)^{\frac{1}{2}}]}{4\tan\alpha}, \tag{2}$$

where α is limited to $|\alpha| < \arctan(1/\sqrt{8}) = 19.5°$. Here the + sign describes diverging waves and the − sign transverse waves. We are here interested in the diverging waves and thus consider only the + sign above. The distance d is the offset distance of the wavestaff array.

2.2. *Nonlinear solitary wave packets*

Nonlinear solitary packets in one and two dimensions have been studied by a number of researchers (see Cohen, Watson & West 1976; Yuen & Lake 1982, and the references cited therein; see also Hui & Hamilton 1979; and Bryant 1984). Tank experiments are discussed in Yuen & Lake (1982). These packets have limited stability when superimposed on a random wave field or when perturbed along the envelope (see §4.2 and §5).

Consider a narrowband wave packet of the form

$$\left.\begin{aligned}\eta(x,y,t) &= \mathrm{Re}\,[\eta_c],\\ \eta_c(x,y,t) &= G(x,y,t)\,\mathrm{e}^{\mathrm{i}(kx-\omega t)},\end{aligned}\right\} \tag{3}$$

where η is the surface displacement, η_c is the complex surface displacement, G is a complex envelope, and $\omega = (gk)^{\frac{1}{2}}$ is the linear wave frequency. The nonlinear Schrödinger equation for G is

$$\mathrm{i}(G_t + c_g G_x) - \frac{\omega}{8k^2}(G_{xx} - 2G_{yy}) - \tfrac{1}{2}\omega k^2 |G|^2 G = 0, \tag{4}$$

where $c_g = \mathrm{d}\omega/\mathrm{d}k$ is the linear wave group velocity. Conventional one-dimensional envelope solitons are obtained by assuming no y-dependence.

To describe oblique, two-dimensional solitary wave packets we refer again to figure 1. The carrier waves with wavevector $\boldsymbol{k}$ observed at P propagate parallel to the x-axis, as implied by (3). The wave packet envelope propagates at right angles to the line S–P, or along the u-axis in the figure. The angle ψ between the u- and x-axes is

$$\psi = \tfrac{1}{2}\pi - \theta - \alpha. \tag{5}$$

We see that

$$u = x\cos\psi + y\sin\psi. \tag{6}$$

The oblique envelope function G is of the form

$$G(x,y,t) = A_0\,\mathrm{sech}\,[mk\left(\frac{2}{\gamma}\right)^{\frac{1}{2}}(u - \cos\psi c_g t)]\exp -\tfrac{1}{4}\mathrm{i}\omega m^2 t. \tag{7}$$

Here A_0 is the amplitude and $m = A_0 k$ is the peak wave slope. The quantity γ is

$$\gamma = \cos^2\psi - 2\sin^2\psi. \tag{8}$$

Both $\frac{1}{2}\pi - \theta$ and ψ are restricted to angles whose tangent is less than $1/\sqrt{2}$. This permits geometric consistency of the oblique solitons and the diverging portion of the linear Kelvin wake.

The frequency of the carrier wave in an envelope soliton is slightly greater than ω. From (3) and (7) the observed frequency ω_0 is

$$\omega_0 = \omega(1 + \tfrac{1}{4}m^2). \tag{9}$$

The increase in ω_0 compared to ω is 1 % or less if the peak wave slope is 0.2 or less. The phase speed of the carrier wave in an envelope soliton is ω_0/k, thus the increase in the phase speed compared to that of a linear wave is the same as the frequency increase. The velocity of the envelope of the soliton is also larger than the linear wave group velocity, but a higher-order expansion than (4) is required to determine the magnitude of the increase. Dysthe (1979) has performed this expansion for a finite-amplitude wavetrain and his results show that the nonlinear increase in the envelope velocity can be larger than the increase in the phase speed. The nonlinear increases

in the frequency, phase speed, and envelope velocity all imply that the kinematics of the carrier waves in a nonlinear ship wake feature will be slightly different from linear Kelvin wake kinematics. However, the variability in our data and the absence of aerial photographs during the period of data collection both preclude a measurement of the small nonlinear changes in the carrier wave kinematics. Accordingly, when analysing wavestaff data, we shall refer to the observed frequency as ω, we shall not correct for the small frequency increase in (9), and we shall use linear Kelvin wake kinematics to determine k, θ, α, and ψ from U and ω.

2.3. *Linear Gaussian wave packet*

If the observed feature were a linear wave packet, its amplitude would decay asymptotically as $1/(\Delta x')^{\frac{1}{2}}$, where $\Delta x'$ is the distance behind the ship. The envelope would spread owing to linear wave dispersion, and the asymptotic spreading rate would be proportional to the initial range of Fourier components that comprise the packet. For convenience, we calculate the evolution of a Gaussian packet (see Kinsman 1974; see also Clauss & Bergmann 1986). In §4 this will be compared with the observed evolution of the solitary feature.

The wave vector has components p and q along the u- and v-axes, respectively (see figure 1). The complex surface displacement has the assumed form

$$\eta_c(x,y,t) = e^{iqv}\int_{-\infty}^{+\infty} dp\, a(p)\, e^{i(pu-\omega t)}, \tag{10}$$

where

$$\omega = g^{\frac{1}{2}}(p^2+q^2)^{\frac{1}{4}} \tag{11}$$

and

$$a(p) = \frac{a_0}{s(2\pi)^{\frac{1}{2}}}\exp\left[\frac{-(p-p_0)^2}{2s^2}\right]. \tag{12}$$

We assume that $s \ll p_0$. Consistency with the geometry of (3) is achieved if we chose p_0 so that

$$kx = p_0 u + qv, \tag{13}$$

where

$$k = (p_0^2+q^2)^{\frac{1}{2}}, \quad p_0 = k\cos\psi. \tag{14}$$

At $t = 0$, (10) may be evaluated as

$$\eta_c(x,y,0) = a_0 \exp(ikx)\exp -\tfrac{1}{2}(s^2u^2). \tag{15}$$

Note that the initial carrier wavelength is uniform. The wave height variance $|\eta_c(x,y,0)|^2$ decays to e^{-1} of its maximum value a_0^2 over a distance

$$\sigma(0) = s^{-1}. \tag{16}$$

The spatial width is defined to be twice this distance ($2\sigma(0)$) and the temporal width is the spatial width divided by the component of the group velocity along the u-axis, $c_{gu} = c_g\cos\psi$.

To evaluate η_c at time t, we calculate the Taylor series for ω about $p = p_0$ and truncate the series at the second-order term. For our purposes this is a reasonable approximation. The result is

$$\omega = \omega_0 + A(p-p_0) + \tfrac{1}{2}B(p-p_0)^2, \tag{17}$$

where

$$A = c_g\cos\psi, \quad B = \frac{c_g}{2k}(2-3\cos^2\psi). \tag{18}$$

Then

$$\eta_c(x,y,t) = \frac{a_0}{(1+is^2Bt)^{\frac{1}{2}}}\exp[i(kx-\omega_0 t)]\exp\frac{-R^2}{2\sigma^2(t)}\exp\frac{is^2BtR^2}{2\sigma^2(t)}, \tag{19}$$

with $$R = u - \cos\psi c_g t. \tag{20}$$

The wave height variance at time $t = \Delta x'/U$ decays to e^{-1} of its maximum over a distance

$$\sigma(t) = \sigma(0)\left(1+\frac{B^2t^2}{\sigma^4(0)}\right)^{\frac{1}{2}}, \tag{21}$$

with $\sigma(0)$ defined in (16). The peak amplitude decays with

$$\text{Max}\,[|\eta_c(x,y,t)|] = a_0\left[1+\frac{B^2t^2}{\sigma^4(0)}\right]^{-\frac{1}{4}}. \tag{22}$$

2.4. *Packet energy*

For future purposes, we define a quantity, which we call the partial energy, that equals the integral of the packet energy between points where the wave height variance is 1/e of its maximum value:

$$E_p = \tfrac{1}{2}g\int_{-\sigma}^{+\sigma}|\eta_c(u,v,t)|^2\,du, \tag{23}$$

$$\sigma: |\eta_c|^2 = e^{-1}\,\text{Max}\,[|\eta_c|^2] \quad \text{at}\, u = \pm\sigma. \tag{24}$$

The total energy E_T is defined as the integral of the packet energy between $\pm\infty$. E_p is convenient for data analysis because we use 2σ as our measure of the packet width. E_T cannot be calulated directly from the data because of the presence of ambient waves.

For the linear Gaussian wave packet, we have

$$\begin{aligned} E_T &= \tfrac{1}{2}\pi^{\frac{1}{2}}g\,\sigma(0)\,a_0^2 \\ &= 0.89\,g\sigma(0)\,a_0^2, \end{aligned} \tag{25}$$

and

$$\begin{aligned} E_p &= \text{erf}\,(1)\,E_T \\ &= 0.75\,g\sigma(0)\,a_0^2. \end{aligned} \tag{26}$$

For the oblique nonlinear solitary wave packet, we have

$$\begin{aligned} E_T &= [\cosh^{-1}e^{\frac{1}{2}}]^{-1}\,g\sigma A_0^2 \\ &= 0.92\,g\sigma A_0^2 \end{aligned} \tag{27}$$

and

$$\begin{aligned} E_p &= (1-e^{-1})^{\frac{1}{2}}E_T \\ &= 0.73\,g\sigma A_0^2. \end{aligned} \tag{28}$$

The half-width σ in (27) and (28) is given by the solution of

$$\text{sech}\left[mk\left(\frac{2}{\gamma}\right)^{\frac{1}{2}}\sigma\right] = e^{-\frac{1}{2}}. \tag{29}$$

When analysing data we shall use the definition

$$E_p = gc_{gu}\int_{t_1}^{t_2}\overline{\eta^2}\,dt \tag{30}$$

in place of (23). t_1 and t_2 are the times when $\overline{\eta^2}$ is e^{-1} of its maximum value. The overbar denotes an average over a time interval that is one wavelength of the carrier wave. When comparing theory and data, we shall ignore the difference between (23)

and (30), which is small if there are at least a few carrier wave wavelengths in the packet (see §4.1). An alternative to (30) is a temporal integral of the same form as (23), with a good estimate for η_c that is obtained by bandpassing 2η over the negative frequencies (Shum & Melville 1984).

3. Field experiment procedures

This section describes the components of the field experiment – the target ship, the wavestaff array, and the experimental data collection procedure.

3.1. *The target ship*

The target ship selection was based on two main criteria. First, the ship had to generate a distinct steep feature inside the Kelvin cusp line, and second, the ship had to be small enough, on the order of 30 m, to manoeuvre at high speed by the ONR Tower. The target ship for the experiment was chosen after an aerial survey of wakes from ships of opportunity including commercial fishing boats and small Navy vessels. The selected target ship was a Point Class Coast Guard cutter (*Point Brower*) with a 25.3 m waterline length, 5.2 m beam, 1.8 m draught, and 69 ton displacement (Jane's 1985). The hull shape is typical of larger surface combatants.

A photograph of the wake of the Coast Guard ship taken during the aerial survey prior to the experiment is shown in figure 2. The photograph shows the steep compact wave group inside the Kelvin cusp line at an angle slightly more than half of the cusp line angle. The steep surface slopes produce the sun glitter along the port side inner feature. The length of each inner feature in the image can be deduced from the number of wave crests along the ray and the values of the parameters in table 1, §4. There are about 40 wavelengths along the starboard ray and 25 wavelengths along the port ray; thus the rays are about 1.1 and 0.7 km long, respectively. The width of each inner feature is clearly increasing for about the first half-kilometre along the ray, while the change in the width is reduced thereafter.

3.2. *The wavestaff array*

The wavestaff array was designed to measure properties of the Kelvin wake features, including wave height, slope, and propagation direction. Sixteen single resistance-wire wavestaffs were selected for the instrument array based on the relative simplicity of deployment and low cost (Flick *et al.* 1979). Since only general characteristics of the target signal were known, the array was designed to provide flexibility for data analysis. A V-configuration was constructed of two rectangular aluminium frames with eight wires in each frame. The frames were mounted at a 60° angle with respect to each other. The overall frame dimensions, 3.05 m long by 2.74 m high, were dictated by weight constraints and handling considerations. The horizontal spacing between the wires varied from 0.15 to 0.60 m, providing a maximum horizontal aperture of 2.29 m as shown in figure 3(*a*). Although a larger array size was desired from data collection considerations, a larger array would be too difficult to manoeuvre around the tower without special equipment. The actual vertical aperture was 2.59 m. The distance between the two end wires of each frame closest to the apex of the V was 0.15 m. Directional slope measurements near the apex were thus available at spacings as short as 0.15 m and 0.13 m in the north–south and east–west directions, respectively.

The vertical structures of the frames were designed to minimize interference with the sea surface and, therefore, to minimize contamination to the wire sensors. This

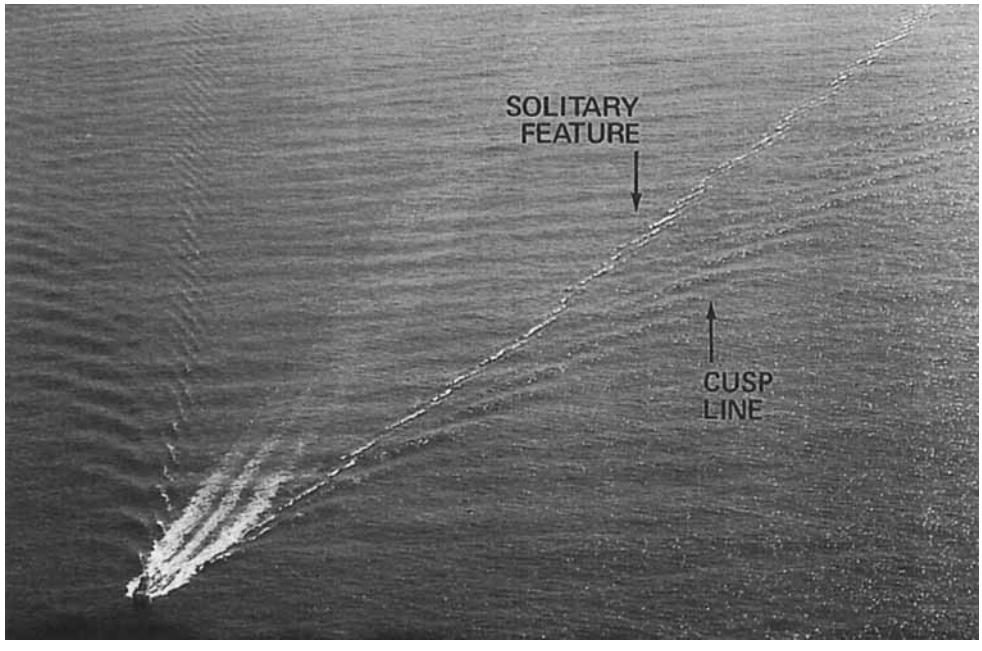

FIGURE 2. Aerial photograph of the wake of the Coast Guard cutter *Point Brower* travelling at 7.7 m/s taken prior to the experiment. The solitary feature is visible inside the 19.5° Kelvin cusp line. The experimentally determined wake half-angle of the feature is 10.9°. As discussed in the text, the lengths of the starboard and port rays in the photo are about 1.1 and 0.7 km, respectively. The width of each feature is increasing for the first 0.5 km, while the change in the width is reduced thereafter.

design included vertical structures with small cross-sections (0.05 m) that were offset from the plane of the array as shown in figure 3(*b*).

The data were sampled at 20 Hz after low-pass filtering in the wavestaff electronics below 5 Hz using a 3-pole Bessel filter. In addition, the data were filtered at 35 Hz in the Data Translation electronics with a single pole filter. The frequency response of the resistance wires is estimated at 2–4 Hz.

The resistance-wire system was calibrated both dry and wet. In order to simulate the sea water return in the dry laboratory calibration, a shorting resistance of about 1.7 Ω was inserted between the measurement location on each wire and its ground return to the frame. Mesurements with the shorting resistance were made at 1 ft. intervals. The mean and standard deviation were computed for 10 s (with a 20 Hz data rate) for each wire. Typical standard deviations were less than 5 mV, or the equivalent of less than 1 mm in height. The system had very low noise characteristics with a resolution on the order of millimetres. The mean values of voltage output versus height were analysed with a least-squares fit routine. The average calibration was 14.02 cm/V. Variation between channels was only about 2%.

The wavestaff was deployed on the west side of the ONR Tower from the cantilevered extension at the south end of the tower with the V opened toward the west. Interference from tower structures was minimal and probably below the noise level of the sensor. The wires were cleaned with a mild hydrochloric acid solution at the beginning of each test day. Although free-floating kelp was sighted in the area of the experiment, no fouling occurred during the data collection.

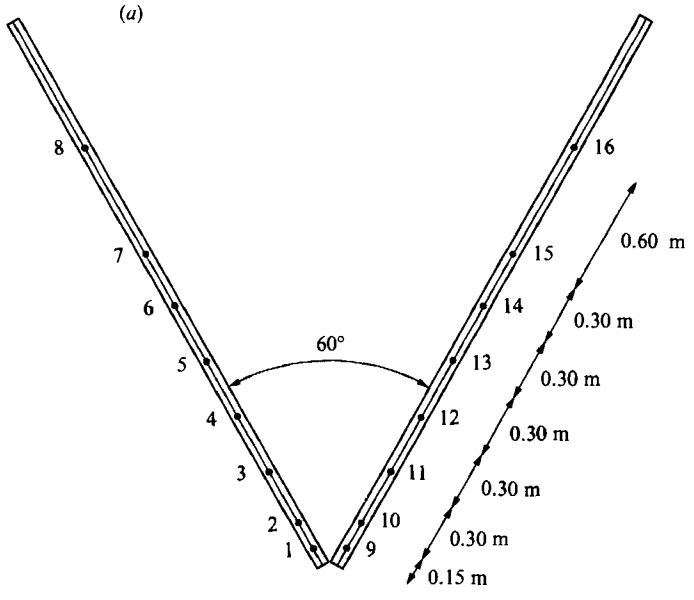

Top view of the wavestaff array

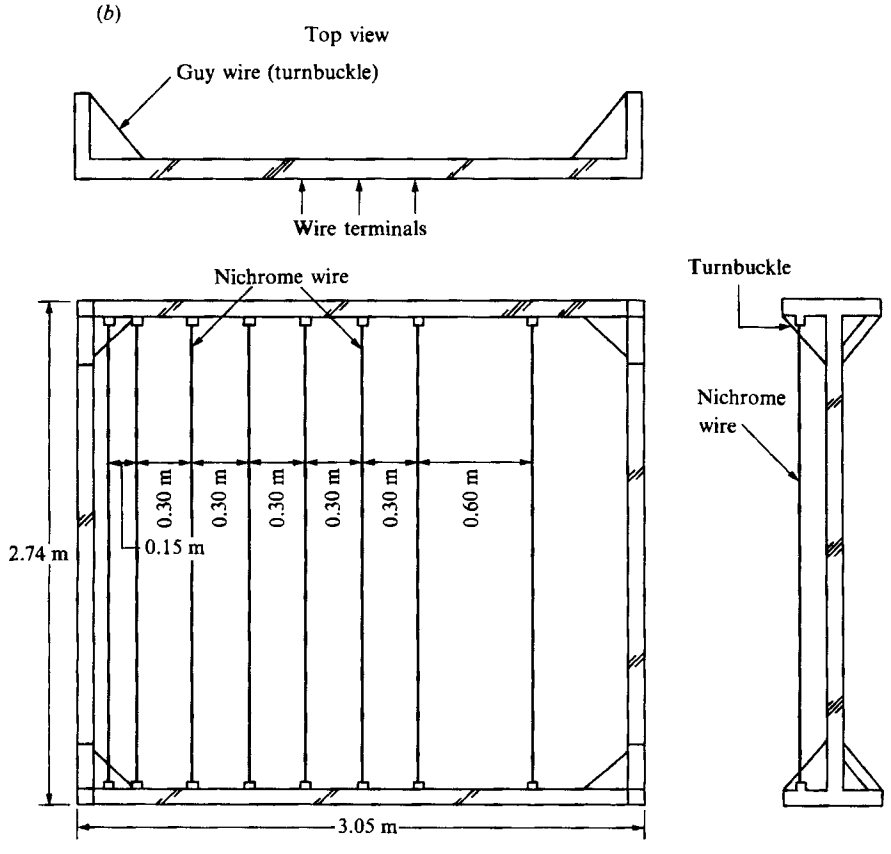

Side view of one side of the array

Side view

FIGURE 3(*a*). Plan view schematic of the V-configuration showing the spacing of the sixteen wires in the wavestaff array. Wires 1–8 have the same wire spacing as wires 9–16. Slope measurements are computed from finite differencing the wave height measured by wires 1, 2, 9, and 10. (*b*) Frame configuration and wire spacing of the wavestaff array.

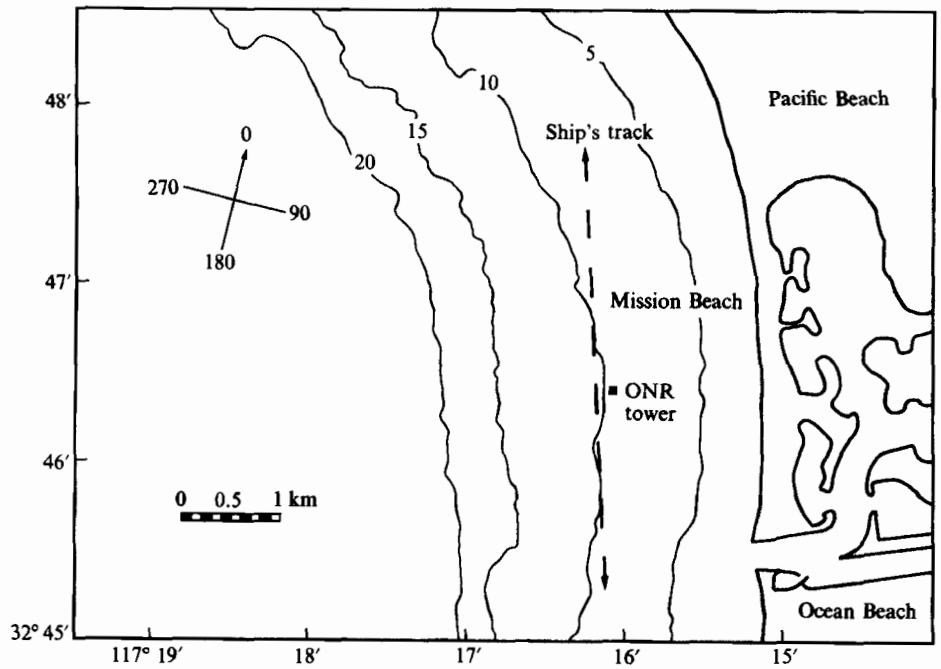

FIGURE 4. Map of the field experiment site showing the location of the ONR Tower. Depth contours are in fathoms.

3.3. *Data collection procedure*

The experiment took place over a period of four days from 11 August–14 August 1986. The run numbers are designated by the day of the data collection – M, T, W, and R for Monday, Tuesday, Wednesday, and Thursday – and by the number of the run each day. Tests were conducted in the mornings, between 7.15 a.m. and 11.30 a.m. local time, to avoid the increase in afternoon sea breeze. Background operating conditions varied over wind speeds of 0–6 m/s with sea states between 0 and 2 and usually less than 0.3 m swell.

The target ship steamed at fixed offset distances (64 m–0.73 km) along a line roughly north–south near the ONR Tower shown in figure 4. The water depth at the tower is 18 m so that deep-water theory applies for the ship waves, which have wavelengths less or equal to the 38 m transverse wavelength when the ship speed is 7.7 m/s. The target runs were designed to vary three parameters – ship's speed, heading, and offset distance from the tower. Target speeds were between 3.6 and 10.3 m/s (7 and 20 knots), corresponding to Froude numbers of 0.23–0.65. The runs were made with either northerly ($\sim 350°$) or southerly ($\sim 170°$) headings and the heading was held constant to within about 10° during each run. Radar and Loran fixes of the range and bearing of the tower were taken from the Coast Guard cutter every 2 minutes. The nominal uncertainty in these radar fixes is about 5 m. The logged ship speed used in the calculations was consistent with the speed inferred from the radar positions to within ± 1 m/s.

Photographs and videotape recordings were made during nearly every run. The time of day was logged during the passage of both the Kelvin wake cusp line and the steep inner feature through the instrument array. Figure 5(*a–d*) shows photographs of the cutter, the feature, and the wavestaff array taken from the ONR Tower.

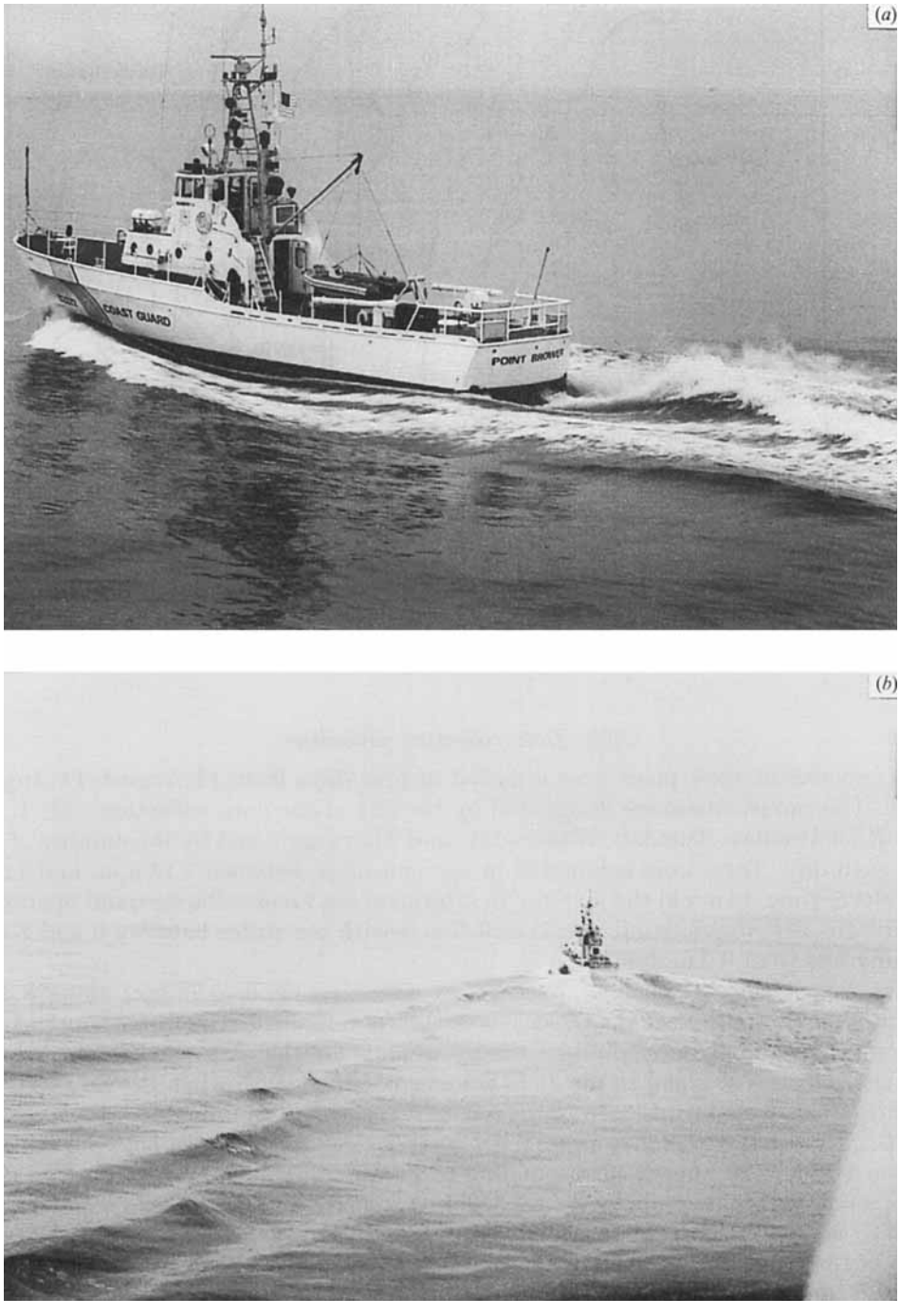

FIGURE 5(*a*, *b*). For caption see facing page.

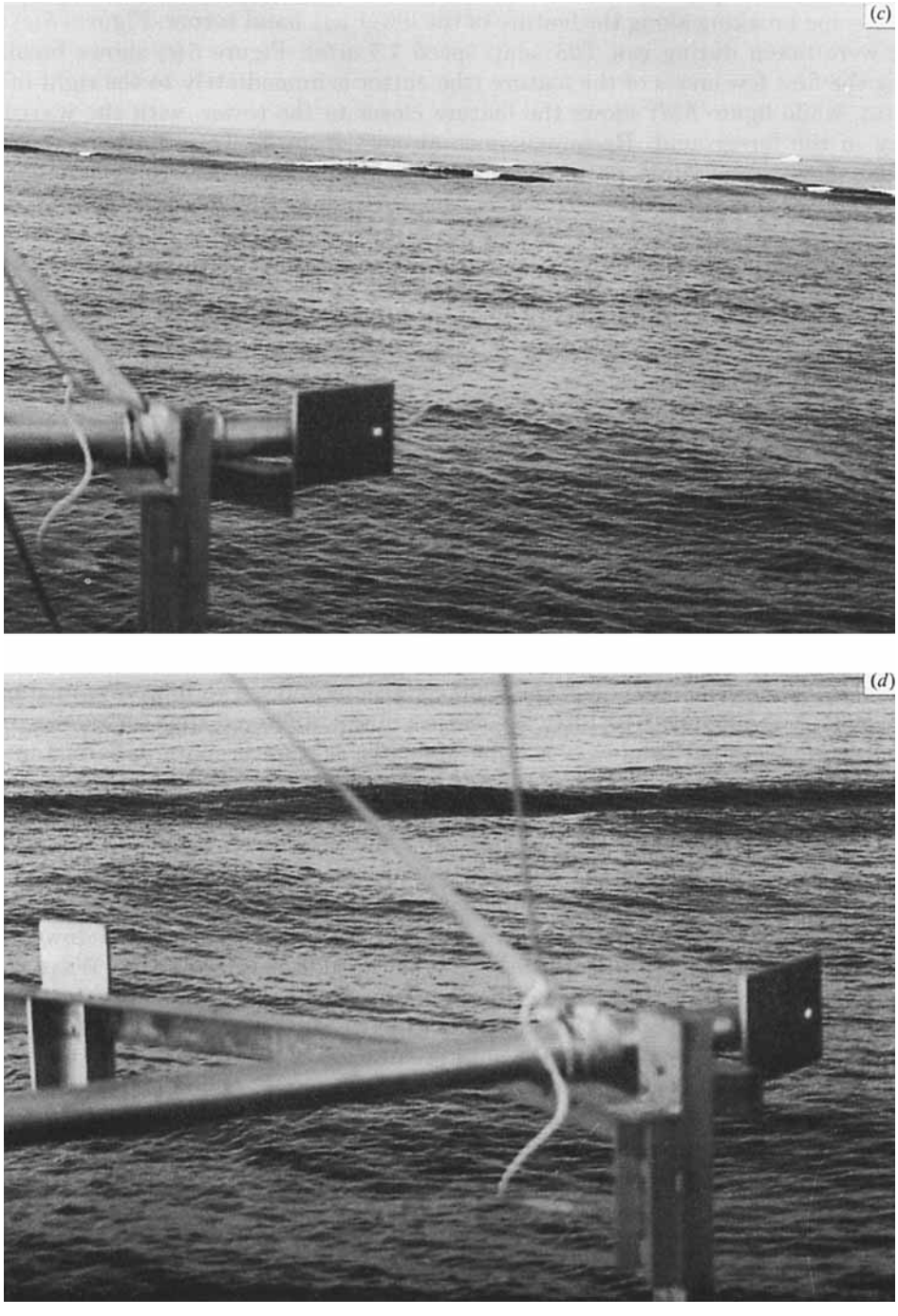

FIGURE 5. (*a*) Photograph taken from the ONR Tower of the Coast Guard cutter *Point Brower* travelling at 7.7 m/s during run M02. (*b*) Sequential photograph after (*a*) showing the inner feature as it passed by the tower. (*c*) Photograph taken from the ONR Tower of the steep inner feature immediately aft of the cutter during run T08. The cutter is immediately to the right of the photo and is travelling at 7.7 m/s. The wavestaff array is in the foreground. (*d*) Sequential photograph after (*c*) showing the inner feature closer to the tower.

Figures 5(*a*) and 5(*b*) were taken during run M02 (ship speed 7.7 m/s). Figure 5(*b*) shows some breaking along the feature in the lower left-hand corner. Figures 5(*c*) and 5(*d*) were taken during run T08 (ship speed 7.7 m/s). Figure 5(*c*) shows breaking along the first few crests of the feature (the cutter is immediately to the right of the photo), while figure 5(*d*) shows the feature closer to the tower, with the wavestaff array in the foreground. Reconnaissance aircraft from El Toro Marine Corps Air Station flew a cloverleaf pattern over the field site each day to record optical photographs and SAR data. However, no SAR data of adequate quality were obtained.

The surface data collection was very successful; a total of 48 traverses of the wake were made with 1, 1, 6, 30, and 9 runs at speeds of 3.6, 4.1, 5.1, 7.7, and 10.3 m/s, respectively. The analysis described in this paper focuses exclusively on the 30 data runs collected at 7.7 m/s (15 knots; Froude number 0.49).

4. Field data analysis

4.1. *Data analysis and theoretical comparison*

The wave height time series were recorded as the ship passed by the tower, beginning approximately when the ship was abreast of the tower. For a given run, the duration of the data collection was determined by the ship offset distance from the tower. The approximate time of passage of the feature through the array was noted for each run during the experiment. Figures 6(*a*) and 6(*b*) show two representative runs from the experiment. The raw wave height time series from Channel #1 of the wavestaff array are plotted in curve (i). Although the wind conditions and sea state were calm during these runs, it is difficult to identify the feature in the unfiltered time series. Since the eye easily detects patterns over a large area, the feature is more apparent in the photo in figure 2 than in a single wavestaff record. The same time series bandpassed between 2.2 and 4.4 rad/s are shown in curve (ii) in these figures. The feature is easily identified at time 110 s and 150 s in runs M05 and W06, respectively. Typical peak wave heights of the feature are between 10 and 20 cm. The temporal series contain roughly twice as many wavelengths per packet as appear in the photo in figure 2 because the phase velocity is twice the group velocity. Crosstrack and downtrack slope time series for the filtered data are shown in curves (iii) and (iv). Wave slope was calculated by finite differencing the filtered wave height data from sensors 1, 2, 9, and 10 near the apex of the wavestaff array. The crosstrack and downtrack directions are approximate since the ship orientation with respect to the wavestaff array was not measured precisely. The feature is more easily identified in the crosstrack slope records because its propagation direction is more nearly crosstrack. The typical peak slope for the feature in these records is 0.1–0.2.

A spectrogram analysis was used to identify the feature in the wave slope records. The spectrogram (Rabiner & Gold 1975) has been used in fields such as speech pattern recognition where the signal frequency changes with time, and it has been applied to surface wave data (Wyatt & Hall 1988). The spectrogram $S(\omega, t)$ is computed from the local Fourier transform of the data $f(t)$ using the definition

$$S(\omega, t) = \left[\frac{1}{2\pi}\right]^2 \left| \int_{-\infty}^{\infty} F(t-\tau) f(\tau)\, \mathrm{e}^{-\mathrm{i}\omega\tau}\, \mathrm{d}\tau \right|^2, \tag{31}$$

where $F(t-\tau)$ is a transform window, ω is frequency, and t is time. The spectrogram shows the wave record's energy distribution in frequency as a function of time. The waves in a linear Kelvin wake measured in calm water would appear along a

continuous curve in frequency and time. Examples of this are given in Wyatt & Hall (1988). However, the Kelvin wake of the Coast Guard cutter is substantially obscured by the ambient wave field; only the inner angle feature appears distinctly in all the data runs.

Figures 7(*a*) and 7(*b*) show the average of the two spectrograms for the two unfiltered slope components. The time segments are 100 s long, centred at the inner angle feature, and the frequencies are between 1 and 8 rad/s. The particular form of F that is used in the spectrogram is a constant-Q form of the minimum four-term Blackman–Harris window with a full width of ten wave periods (Harris 1978, equation (33)). In all four spectrograms the solitary feature is located near 3.3 rad/s, although its shape varies. Ambient waves and other Kelvin wake components appear at other frequencies. These are particularly evident relative to the solitary feature in record M05. We note that the transverse waves for a ship travelling at 7.7 m/s would have a frequency of 1.3 rad/s. On the sides of the spectrogram are plotted the smoothed variance and the smoothed spectrum which have been obtained by integrating the spectrogram over frequency and time, respectively (the latter integral is divided by 2π). The smoothed variance is one-fourth of the local slope variance – a factor of one-half appears because the function is the average of the variances of the components and an additional factor of one-half appears because the integration is over only the positive frequencies.

We note that the widths of the features in figures 7(*a*) and 7(*b*) are larger than the actual widths. The e^{-1} width of the smoothing filter is about 6 s (Wyatt & Hall 1988), thus if the actual width is Δt, the smoothed width will be roughly $(\Delta t^2 + 6^2)^{\frac{1}{2}}$. A typical Δt is 6 s (see below), for which the smoothed width is 41% larger. Since this is a substantial increase, we restricted the use of spectrograms to feature identification and frequency measurement. Bandpassed wave height data were used to determine the width, energy, and amplitude (see below).

Spectrums were computed for each of the 7.7 m/s traverses with offset distances varying between 64 m and 0.73 km from the tower. The frequency of the wave packet was determined from a weighted average of ω over the feature in each spectrogram (weighted by $S(\omega, t)$); the values for the runs are listed in table 2. The mean frequency of the wave packet for the 24 runs beyond 0.5 km aft is $\omega = 3.28 \pm 0.04$ rad/s, where the error is the standard deviation of the mean. The average kinematical parameters of the solitary feature were determined from the linear theory using $U = 7.7$ m/s and the mean value of ω, and are listed in table 1. The wavenumber determined from linear theory is $k = \omega^2/g = 1.10\ \mathrm{m}^{-1}$. Since the feature is stationary in the ship reference frame, the wavenumber in the direction of the ship track is given by $k'_x = \omega/U = 0.426\ \mathrm{m}^{-1}$ for a ship speed of 7.7 m/s. The crosstrack wavenumber k'_y satisfies $(k^2 - k'^2_x)^{\frac{1}{2}} = 1.01\ \mathrm{m}^{-1}$ and the propagation angle is $\theta = \arctan(k_{y'}/k_{x'}) = 67.2°$. The wake half-angle $\alpha = 10.9°$ is determined from (2), while (5) yields $\psi = 11.9°$. The linear group velocity $c_g = \mathrm{d}\omega/\mathrm{d}k$ is 1.49 m/s. As explained at the end of §2.2, we have not corrected these kinematical parameters for small nonlinear effects.

In the analysis described below, the derived quantities for each run (distance aft, spatial width of the feature, etc.) were calculated from the observed quantities (offset distance from the tower, temporal width of the feature, etc.) using kinematical parameters that were obtained from linear theory, with $U = 7.7$ m/s and with ω given by the observed frequency for each run as listed in table 2. The formula that we used for these kinematical parameters were the same as those listed in table 1 for the average kinematical parameters. In addition, before analysis, each time series of the feature was converted to a locally averaged variance by bandpass filtering

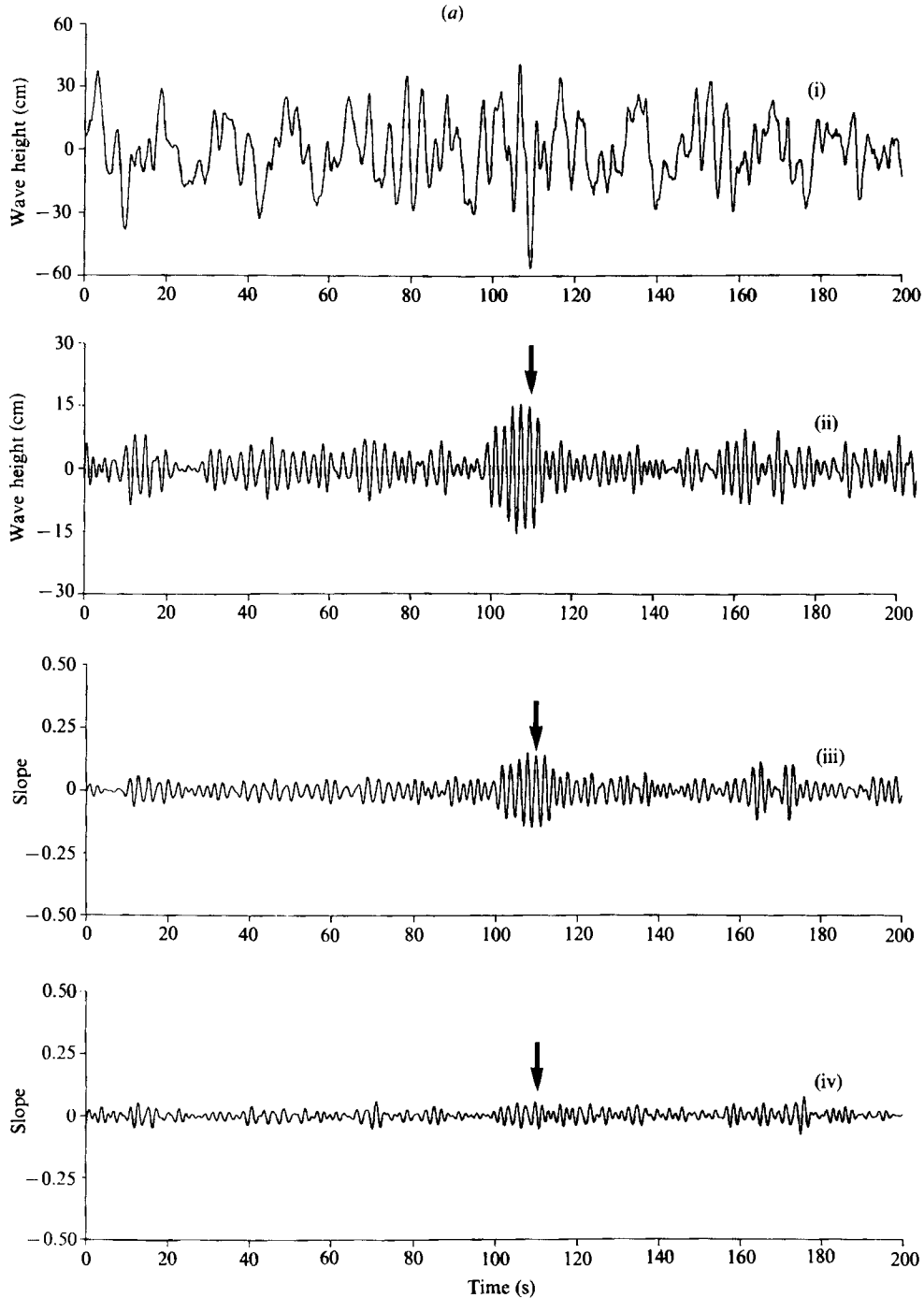

FIGURE 6(a). For caption see facing page.

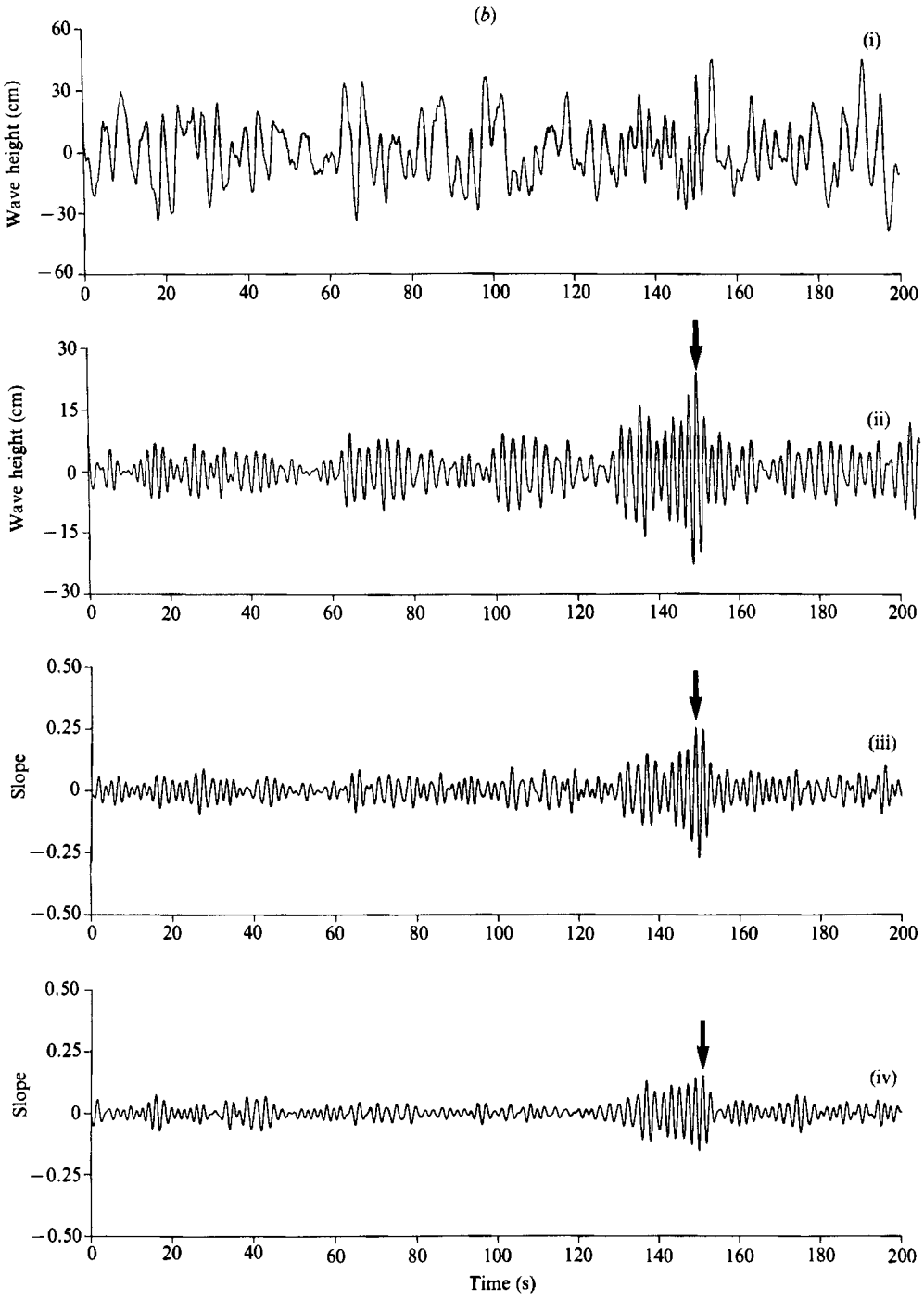

FIGURE 6. (*a*) Run M05; (*b*) run W06. Curve (i) Raw wave height (20 Hz) measured by wavestaff Channel no. 1 (mean set to zero). Curve (ii) Wave height bandpass filtered between 2.2 and 4.4 rad/s. Feature designated by arrow. Curve (iii) Crosstrack waveslope calculated from finite differencing the filtered wave height at sensors no. 1, 2, 9, and 10. Curve (iv) Filtered downtrack wave slope.

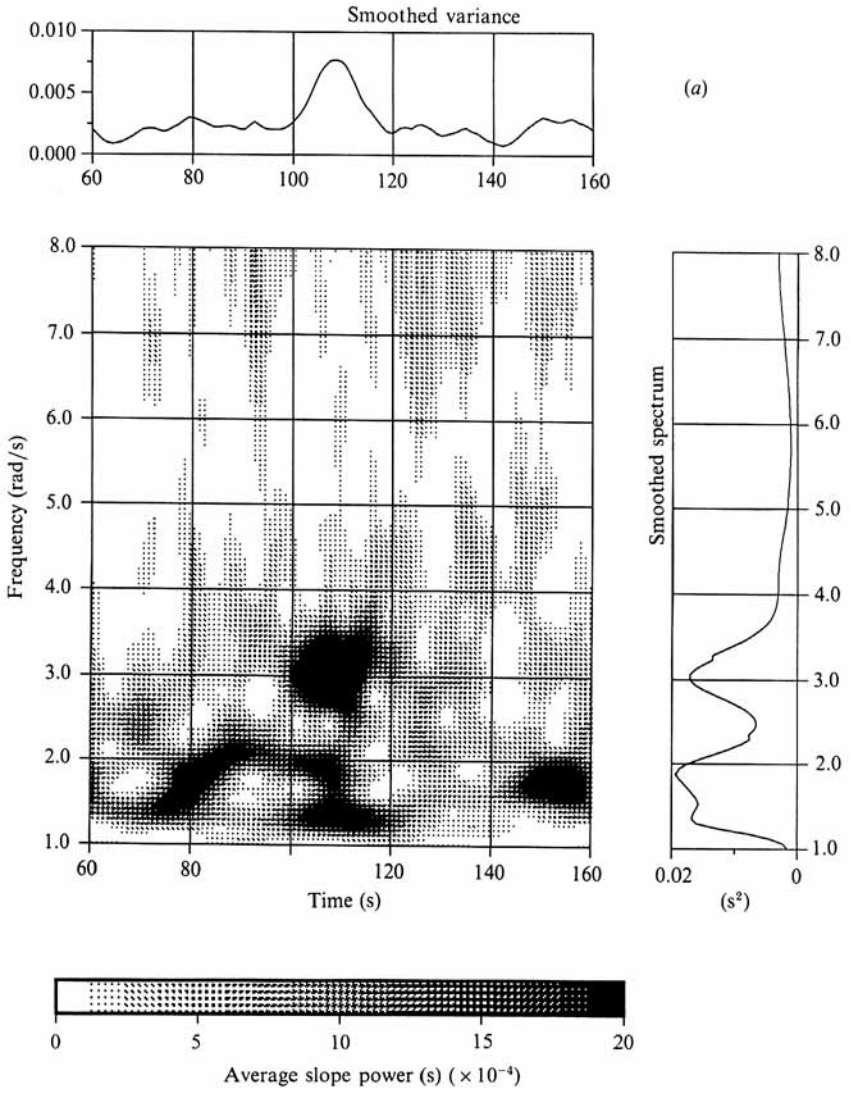

FIGURE 7(*a*). For caption see facing page.

between 2.2 and 4.4 rad/s, squaring, and smoothing with a running mean filter over one period of the carrier wave. The period was determined from the observed frequency for each run listed in table 2. We note that the running mean filter changes the width of the feature by a small amount: theoretical calculations show that for a hyperbolic secant soliton with the observed average characteristics, the average width is increased by 2%, and there is an additional $\pm 3\%$ variance depending upon the phase of the carrier wave with respect to the envelope. We have chosen not to correct for these small changes. We also note that bandpasing eliminates any bound harmonics from the signal, thereby facilitating comparison with the expressions in §§2.2 and 2.3, which do not contain bound harmonics. The bandpassed frequency interval is two-thirds of the average frequency of the wave packet and is wide enough that less than 1% of the energy of the fundamental wave has been filtered out for most of the runs.

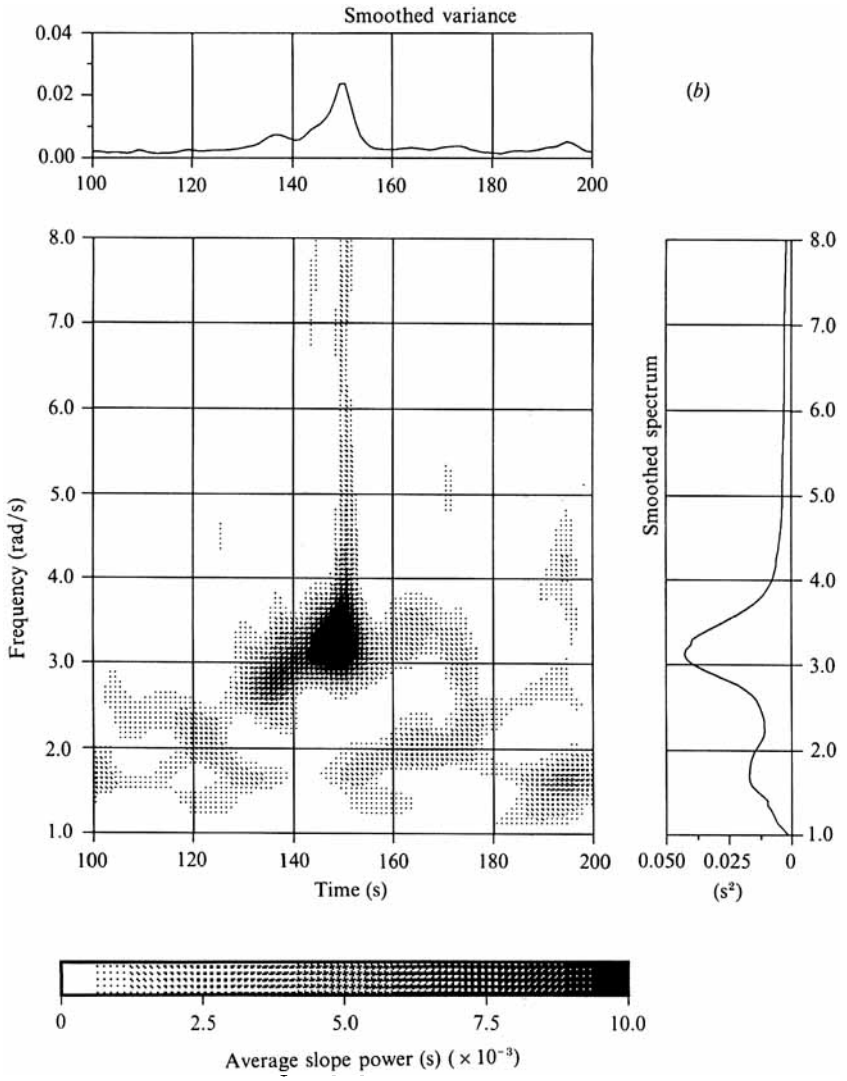

FIGURE 7. (*a*) Spectrogram of run M05 computed from the unfiltered slope time series. The feature is centred at 110 s in time and at 3.09 rads/s in frequency. The grey scale varies from 0 to 20×10^{-4} s. The last bin also contains all values $> 20 \times 10^{-4}$ s. The low-frequency energy below 2.2 rad/s is due to ambient swell or to the transverse Kelvin wave in the wake. (*b*) Spectrogram of run W06 computed from the unfiltered slope time series. The feature appears near 150 s in time and 3.34 rad/s in frequency. Again there is little low-frequency energy.

Figure 8 is a comparison of all of the bandpassed wave slope variance records of the feature. The figure shows a plot of the total slope variance as a function of the crosstrack distance from the wake half-angle $\alpha = 10.9°$. The vertical axis shows the distance behind the ship for each run which is defined as $d \cot \alpha$, where d is the observed offset distance of the wavestaff array and α is the wake half-angle for each run calculated using the formula shown in table 1. For each feature, the crosstrack distance from this ray was calculated from the distance behind the ship and the observed frequency of each feature, under the assumption that the wake geometry was given by linear Kelvin wave theory. The time in the wave record was converted to effective crosstrack distance by multiplying by $-c_g \sin \theta$, where c_g and θ were the

$U = 7.7$ m/s (15 knots)	ship speed
	Observed parameters
Average of 24 runs beyond 0.5 km aft, with standard deviation of the mean:	
$\omega = 3.28 \pm 0.04$ rad/s	frequency of solitary feature
$2\bar{\sigma} = 8.9 \pm 0.7$ m	spatial width of solitary feature at 1/e of the peak wave height variance
$\bar{E}_p = 0.75 \pm 0.07$ m^4/s^2	partial energy of solitary feature (see (30))
$\bar{A}_0 = 15.2 \pm 0.7$ cm	peak wave amplitude
Parameters calculated from linear Kelvin wake theory using U and mean value of ω	
$k = \frac{\omega^2}{g} = 1.10$ m^{-1}	wavenumber
$\lambda = \frac{2\pi}{k} = 5.72$ m	wavelength
$k_{x'} = \frac{\omega}{U} = 0.426$ m^{-1}	wavenumber in downtrack direction
$k_{y'} = (k^2 - k_{x'}^2)^{\frac{1}{2}} = 1.01$ m^{-1}	wavenumber in crosstrack direction
$\theta = \arctan\left(\frac{k_{y'}}{k_{x'}}\right) = 67.2°$	propagation angle with respect to ship track
$\alpha = 10.9°$	wake half-angle (calculated using (2))
$\psi = \frac{1}{2}\pi - \theta - \alpha = 11.9°$	envelope angle with respect to carrier wave
$\gamma = \cos^2\psi - 2\sin^2\psi = 0.873$	
$c_g = \frac{d\omega}{dk} = 1.49$ m/s	group velocity
$c_{gu} = c_g \cos\psi = 1.46$ m/s	component of group velocity in u-direction

TABLE 1. Parameters for solitary feature

values for each run. The peak slope variances are in the range 0.01–0.03 and the features appear at angles between 10°–12°. The three curves at the farthest distance from the vehicle are of slightly lower amplitude. The scatter between the runs can be due to a variety of effects, as discussed in §4.2. Some variability in the feature is apparent in figure 2.

The width of the feature was calculated from the bandpassed wave height variance records. The temporal width of the feature was chosen as the time interval between the points where the variance was 1/e of its maximum. The spatial width, 2σ, is defined as the temporal width times c_{gu}, where c_{gu} is given by the value for each run calculated using the formula shown in table 1. An average was taken of the values from the sixteen wavestaffs in each run. The results are listed in table 2.

Figure 9 compares the linear dispersion of a Gaussian wave packet from (21) to the feature widths measured from the experimental data. The data are plotted as packet width 2σ versus the distance behind the ship. At $t = 0$, the frequency of the carrier wave in the linear wave packet is assumed to be 3.28 rad/s and ψ is assumed to be 11.9°. The spreading in a linear packet is determined by its initial width. An initially narrow packet, which contains a wide range of Fourier components, will spread more rapidly than one which is initially broader. The curves plotted in figure 9 correspond to Gaussian wave packets with initial widths between 3 and 15 m. The observed packet width remains centred on about 9 m for distances 1–4 km behind the ship. The average width of the feature is 8.9 m, excluding the runs closest ($\leqslant 0.5$ km) to the ship. Although there are fewer experimental data points at the greater offset

Run	Distance aft (km)	Carrier frequency ω(s)	Width 2σ(m)	Partial energy E_p(m^4/s^2)	Amplitude A_0(cm)	Noise estimate $\overline{\eta^2}$(cm^2)
R14	0.35	3.47	7.42	0.64	15.5	7.5
M02	0.40	3.30	7.11	1.02	20.0	10.5
T03	0.41	3.56	5.40	0.90	21.6	27.4
T02	0.43	3.34	6.51	1.32	23.8	17.7
M09	0.47	3.29	6.69	1.01	20.5	7.2
M10	0.50	3.65	4.88	0.68	19.7	9.6
T09	0.87	3.35	4.72	0.84	22.3	19.8
M05	0.87	3.09	15.87	1.32	15.3	15.0
T08	0.97	3.35	5.41	0.59	17.5	11.2
R06	0.97	3.35	8.09	1.26	20.9	9.3
R13	0.98	3.30	8.50	0.45	12.2	4.9
M06	0.99	3.71	6.24	0.11	7.0	10.5
R07	1.03	3.49	6.54	0.49	14.5	14.5
T11	1.32	3.38	7.16	0.89	18.6	12.8
M08	1.40	3.68	4.59	0.20	11.0	11.0
M07	1.41	3.27	8.61	0.77	15.8	14.3
R09	1.44	3.50	5.32	0.36	13.8	12.6
R12	1.44	3.33	6.16	0.39	13.3	9.9
T10	1.45	3.08	9.15	0.57	13.2	11.2
R08	1.58	3.33	11.66	0.51	11.1	7.4
W07	1.61	2.75	17.68	1.31	14.4	15.4
M03	1.73	3.12	14.20	0.93	13.5	10.3
M04	1.74	3.27	11.64	0.76	13.5	9.9
W09	1.79	3.11	11.06	0.89	15.0	17.2
W06	1.81	3.34	7.34	1.16	21.0	18.0
W08	1.83	3.22	10.85	1.23	17.8	18.8
T05	2.44	3.23	8.29	1.02	18.6	11.6
T04	3.12	3.07	7.44	0.44	12.9	18.4
T07	3.48	3.28	5.99	0.60	16.7	10.8
T06	3.56	3.10	11.12	0.93	15.3	15.8

TABLE 2: Data summary

distances, this comparison indicates that the feature in the Coast Guard ship wake does not spread according to linear theory beyond 1 km aft. The somewhat lower value of the observed width at 0.5 km aft is consistent with figure 2, which shows that the width of the feature is increasing for about the first 0.5 km aft.

Figure 10 shows the observed partial energy E_p in the feature as a function of distance behind the ship. The energy was calculated according to (30) by integrating the wave height variance between times when it was e^{-1} of its peak value. The value of c_{gu} that was used in (30) was the value for each run. Each value of E_p is an average of the values from the sixteen wavestaffs in each run. The average of the values of E_p, excluding those at the closest distance ($\leqslant 0.5$ km), is $\bar{E}_P = 0.75 \pm 0.07$ m^4/s^2.

Figure 11 compares the peak amplitude of the feature and the peak amplitude of linear Gaussian wave packets with different initial widths. We chose not to obtain the peak amplitude of the feature directly from the wave height data because of the contribution of the ambient wave field to the peak values (see figure 6). Instead, the peak amplitude was calculated from the observed half-width σ and the observed partial energy E_p using (28). (As can be seen by comparing (26) and (28), the relationship between the peak amplitude and σ and E_p is not sensitive to the exact form of the packet.) The average of the values, excluding those at the closest distance

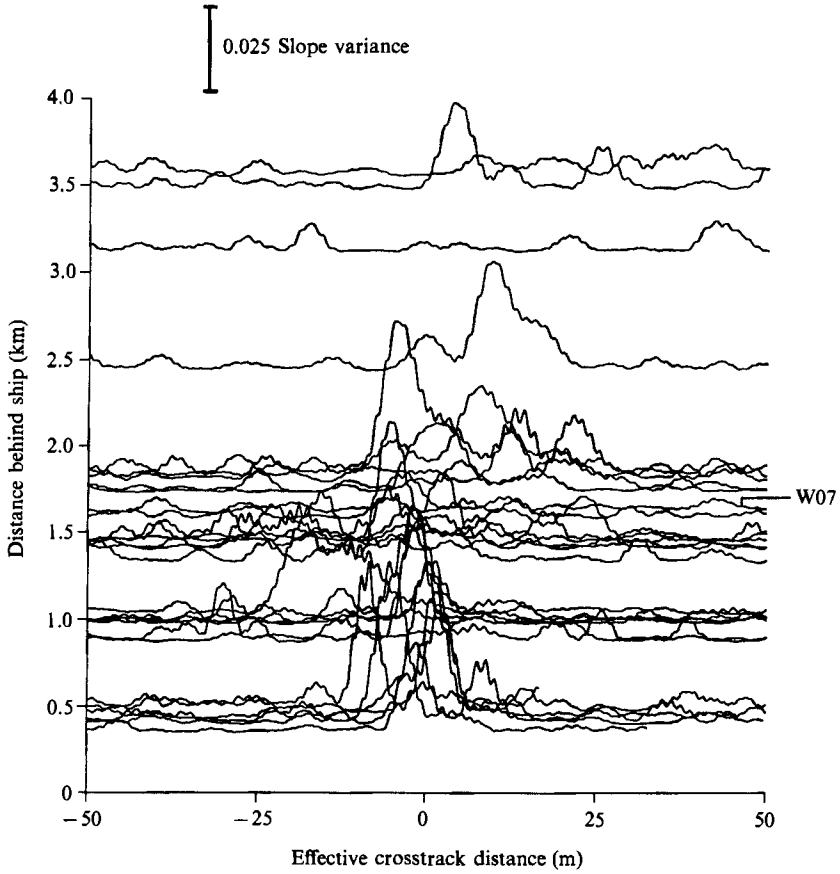

FIGURE 8. Wave slope variance computed from finite difference of the wave height time series bandpass filtered between 2.2 and 4.4 rad/s. The wave slope series were squared and smoothed with a running mean filter over one period of the carrier wave. Effective crosstrack distance is defined in §4.1. The feature in run W07 is off the right-hand side of the figure.

($\leqslant 0.5$ km) is $\bar{A}_0 = 15.2 \pm 0.7$ cm. The peak amplitude of each linear Gaussian wave packet was calculated in two steps. First, a_0 was calculated from (26) using the specified initial width $2\sigma(0)$ and the average value of the observed partial energy $\bar{E}_p = 0.75\ \mathrm{m}^4/\mathrm{s}^2$. Second, the peak amplitude as a function of time was calculated from (22) using a_0, $\sigma(0)$, and the value of B obtained from the parameters in table 1.

The variables plotted in figures 9–11 are listed in table 2. The observed average values $2\bar{\sigma}$, $\bar{E}_p$, and $\bar{A}_0$ are listed in table 1.

The observed average values of $\bar{E}_p = 0.75\ \mathrm{m}^4/\mathrm{s}^2$ and $\bar{A}_0 = 15.2$ cm can be compared to theoretical values predicted from the observed average value $2\bar{\sigma} = 8.9$ m and (28) and (29). We use $\bar{\sigma}$ and the theoretical expression for the envelope of an oblique nonlinear solitary wave packet, (29), to obtain the predicted value $\bar{A}_0 = 13.4$ cm. We use $\bar{\sigma}$ together with the predicted value of $\bar{A}_0$ and (28), to obtain the predicted value $\bar{E}_p = 0.57\ \mathrm{m}^4/\mathrm{s}^2$. The observed $\bar{E}_p$ is 1.3 times the predicted $\bar{E}_p$ and the observed $\bar{A}_0$ is 1.1 times the predicted $\bar{A}_0$.

The fractional increases of 0.3 and 0.1 in the observed values of $\bar{E}_p$ and $\bar{A}_0$ compared to the predicted values are partly due to the effect of ambient waves. To estimate this effect we first obtained an estimate of the ambient waves by calculating

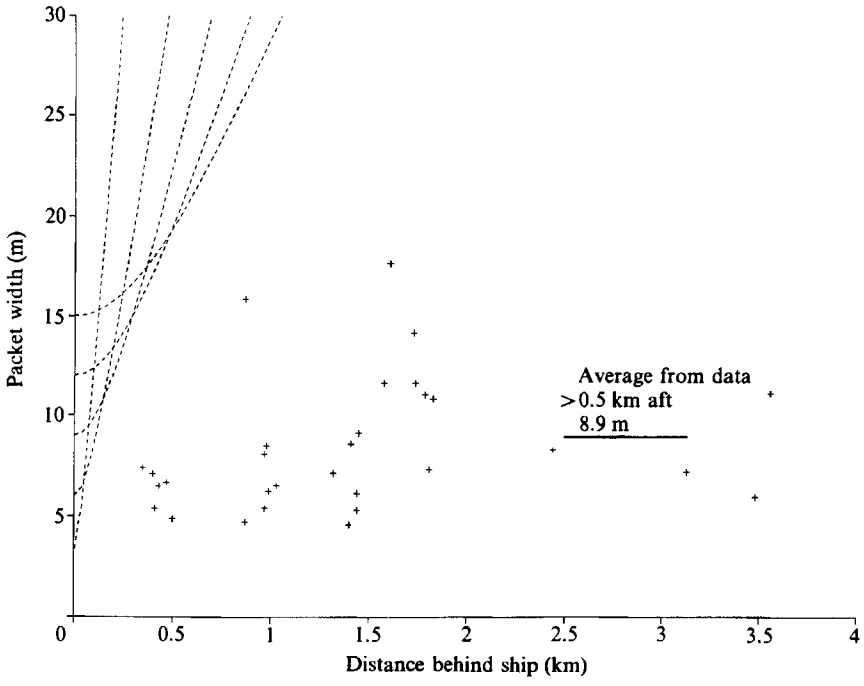

FIGURE 9. Comparison of the measured width of the soliton-like feature and the theoretical widths of linear Gaussian wave packets with various initial widths. The solid line, 8.9 m, is the average of the data values beyond 0.5 km.

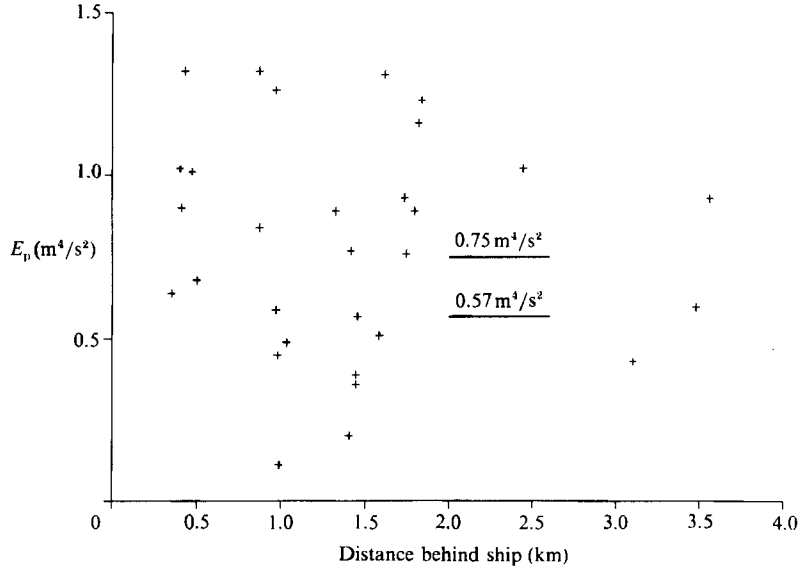

FIGURE 10. The measured partial energy E_p. The average of the points beyond 0.5 km is 0.75 m^4/s^2, while the theoretically predicted value calculated using the average width is 0.57 m^4/s^2.

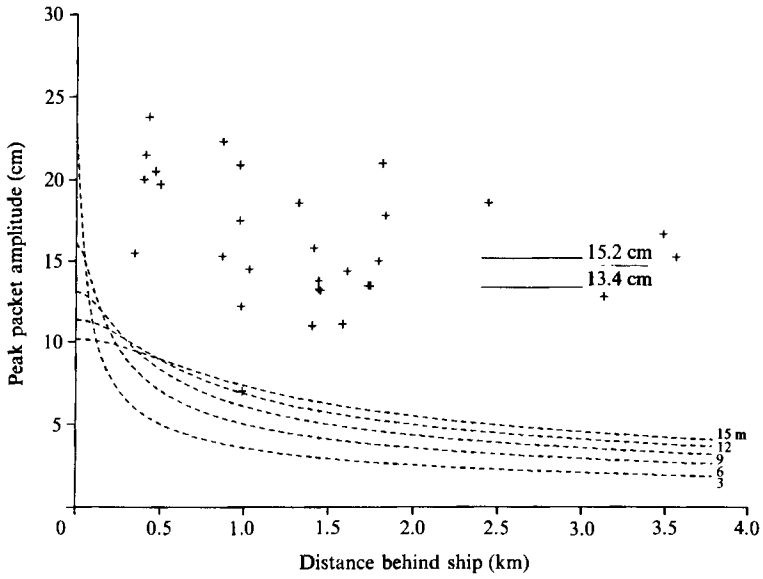

FIGURE 11. Plot of peak amplitude data. The average of the points beyond 0.5 km is 15.2 cm, while the theoretically predicted value calculated from the average width is 13.4 cm. The curves are those predicted for linear Gaussian packets of initial widths between 3 and 15 m and a partial energy equal to the observed average.

the average wave height variance within the 2.2–4.4 rad/s bandwidth for a 50 s time interval after each solitary feature. The values are listed in table 2. The ambient wave field appears to be larger than the ship wave field in this interval. The average of the values over the 24 runs beyond 0.5 km aft is 13 cm^2, which is an r.m.s. wave height of 3.6 cm. We define a noise-to-signal ratio, ϵ, as the ratio of the average ambient wave height variance to the average wave height variance of the soliton near its peak, $\frac{1}{2}A_0^2$. We can only estimate ϵ because we do not know how much of the 13 cm^2 wave height variance is due to ship waves. If we let A_0 be 15.2 cm and if we assume that the entire 13 cm^2 variance is due to ambient waves, then we estimate that ϵ is about 0.1. For $\epsilon \ll 1$, it is straightforward to show that random ambient waves will yield fractional increases of 1.0ϵ, 1.9ϵ, and 0.4ϵ, respectively, in the observed average values of $\bar{\sigma}$, $\bar{E}_p$, and $\bar{A}_0$ compared to the exact values for the soliton. The fractional increase in $\bar{\sigma}$ will yield fractional decreases of -1.0ϵ in the predicted values of $\bar{E}_p$ and $\bar{A}_0$ compared to the exact values for the soliton, if the predicted values are calculated as described in the previous paragraph. The fractional increase in the ratio of the observed $\bar{E}_p$ to the predicted $\bar{E}_p$ will be 2.9ϵ, and the fractional increase in the same ratio for $\bar{A}_0$ will be 1.4ϵ. If $\epsilon = 0.1$, these fractional increases are 0.3 and 0.1, respectively, which are the same values obtained in the previous paragraph.

Before summarizing this section, we review the three systematic effects inherent in the observed and derived quantities that, for reasons explained earlier, we have not corrected for. First, small nonlinear effects change the formula for calculating the kinematical parameters from U and the observed frequency. Second, the smoothing of the variance by the running mean filter increases the packet width by a small amount. Third, the ambient waves increase the observed average values of $\bar{\sigma}$, $\bar{E}_p$, and $\bar{A}_0$. Finally, we reiterate that bandpassing has eliminated the bound harmonics from the signal that we have analysed.

In summary, the analysis in this section shows that the steeply peaked feature in the wake of the Coast Guard cutter is nonlinear. The wavestaff records show less spreading than predicted by linear dispersion between 1 and 4 km aft of the ship. The average amplitude of the feature is 1.1 times the theoretical amplitude for the envelope of an oblique nonlinear solitary wave packet with the observed width. Given the uncertainty in the experimental observations and the variability in the structure of the feature from run to run, the characteristics of the feature between 1 and 4 km aft are consistent on average with those of an oblique nonlinear solitary wave packet, but additional research is needed to understand the variability.

4.2. *Variability*

The variability in figures 8–11 could be due to a variety of effects: superposition of ambient waves; variations in ship speed or heading; time-dependent ship motions; interaction of the feature with the transverse Kelvin wave or with ambient waves or currents; time-dependence or instability of the feature; or dispersive parts of the feature.

As an illustration of the type of variability that can occur along the feature, we show figure 12. This photograph was taken prior to the experiment during the same aerial survey as figure 2, with the cutter travelling at 7.7 m/s. From the photograph and the parameters in table 1, we estimate that the portion of the ray shown in the photograph extends from about 0.7 to 1.9 km aft of the cutter. This is done as follows. From table 1 we note that the average crosstrack wavelength of the carrier waves in the soliton is 6.2 m. Along the bottom of the photograph there are about 18 crosstrack wavelengths between the centre of the solitary feature and the outer part of the cusp line feature; thus, the physical distance is about 112 m. Since the centre of the solitary feature is 10.9° from the centreline (see table 1) and the cusp line is at 19.5°, simple trigonometry implies that the bottom of the photo is about 0.7 km aft of the ship. Along the solitary feature there are about 45 wavelengths of the carrier wave. From table 1 we calculate that the average wavelength of the carrier wave along the solitary feature is 27.7 m; thus the distance from the bottom of the photo to the top is about 1.2 km. This implies that the top of the photo is about 1.9 km aft.

Since there are about 10–12 fluctuations along the portion of the solitary feature shown in figure 12, we estimate that the average wavelength of the sinuous fluctuation is about 0.1 km. Comparing the amplitude of the fluctuation of the wavelength of the carrier wave, we estimate that the amplitude is roughly $\pm 2\lambda$ or ± 11 m. Although the sinuous feature appears in other photos, we do not have a large number of far-field photos of the feature, so we do not know how representative this photo is.

The regularity of the fluctuation suggests that it could be due to the sinuous instability of the oblique nonlinear solitary wave packet. A number of researchers have examined the linear stability of the plane envelope soliton ((7) with $\psi = 0$) to two-dimensional perturbations (see Cohen *et al.* 1976; Yuen & Lake 1982, and the references cited therein). Saffman & Yuen (1978) have pointed out that the stability results for the oblique envelope soliton can be obtained from those of the plane envelope soliton with a geometrical scaling. For an oblique soliton with $2\bar{\sigma} = 8.9$ m, with the carrier wavelength $k = 1.10\ \mathrm{m}^{-1}$ and with the envelope angle $\psi = 11.9°$, the most unstable mode is a stationary sinuous mode with a wavelength of 52 m and an e-folding time of 86 s. This e-folding time corresponds to a distance aft of 0.7 km at a ship speed of 7.7 m/s. The e-folding distance is consistent with the photograph, but the wavelength is half the observed value. The difference could be due to a tendency

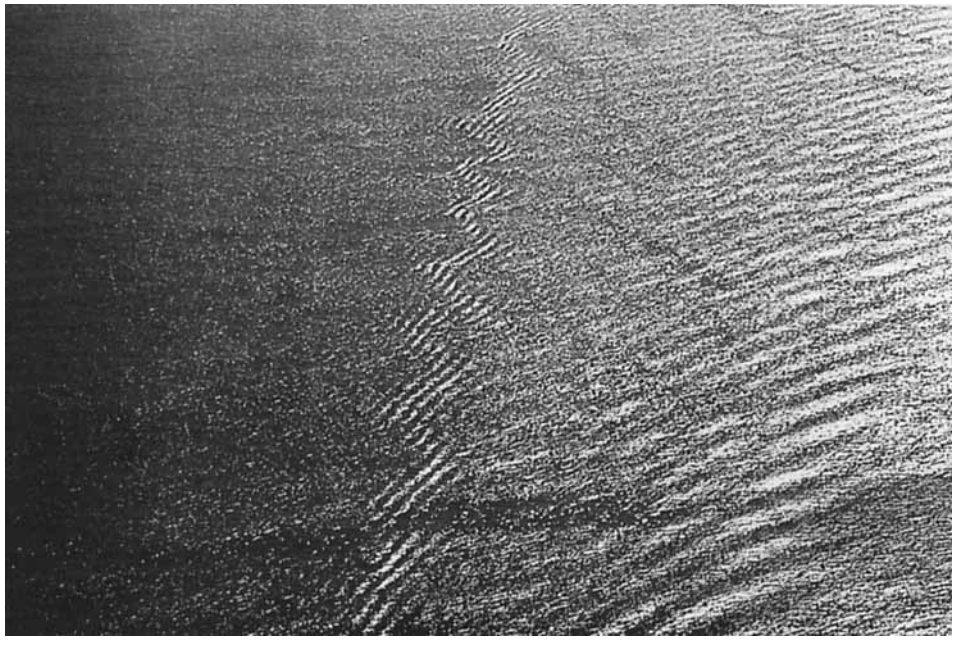

FIGURE 12. Photograph of port side of wake taken during the same aerial survey as figure 2. As discussed in the text, the photograph extends from about 0.7 to 1.9 km aft. The average wavelength of the sinuous fluctuation along the solitary feature is about 0.1 km and the amplitude is roughly ± 11 m.

toward longer-wavelength fluctuations in the initial conditions or to limitations in the applicability of the linearized stability theory. We note that the growth rate maximum in the linearized theory is fairly broad: the e-folding distance aft for a sinuous fluctuation with a wavelength of 0.1 km is 1.0 km.

An alternative explanation for the sinuous fluctuation is a regular variation in the carrier wave frequency induced by any of the effects listed in the first paragraph of this section. If the magnitude of the variation were about $\pm 5\%$ and if it occurred at the cutter or within the first few hundred metres aft, then the variation in the group velocity would be sufficient to yield the observed fluctuation in the position of the ray. There could be some overlap between this alternative explanation and the sinuous instability because a variation in the carrier wave frequency could be an important factor in the instability. We note that the analysis in §4.1 showed a standard deviation of $\pm 6\%$ in the run-to-run variation of the observed frequency, which is consistent with random sampling along a sinuous fluctuation that contains a frequency variation. However, caution must be exercised when comparing the variability in the data to the sinuous fluctuation in figure 12, because the ambient conditions varied during the data runs and differed from the ambient conditions at the time the photo was taken.

It is worth re-examining the data to see whether some of the variation in the dimensions of the feature can be explained by variation in the carrier wave frequency. This type of relationship would be expected if the run-to-run variation was due to sampling along the type of sinuous fluctuation described in the previous paragraph. For an oblique solitary wave packet, the relationship between the width,

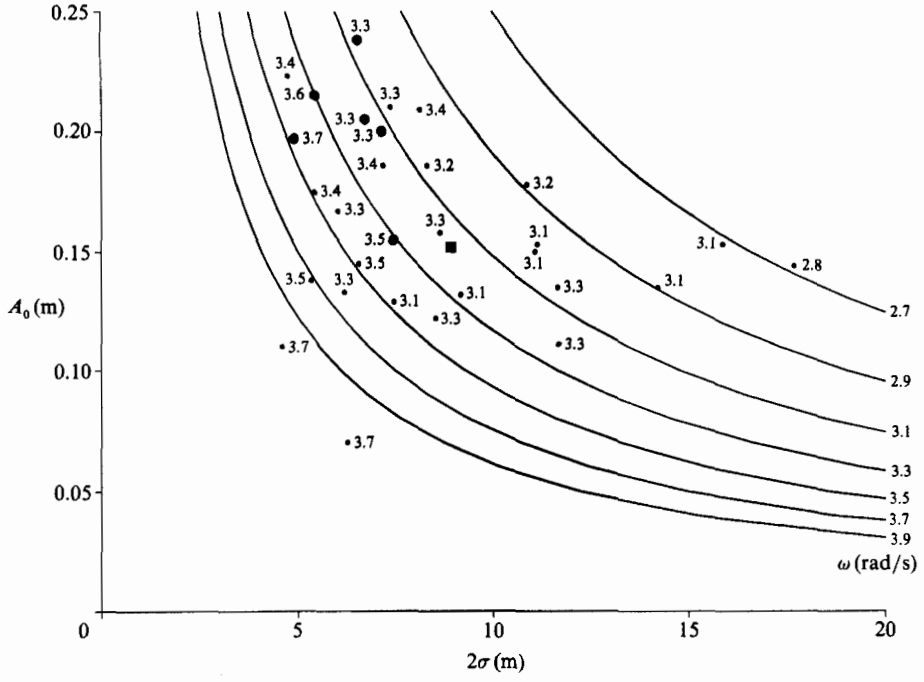

FIGURE 13. Plot of observed amplitude versus observed width. Larger points are $\leqslant 0.5$ km aft. The square is the observed average. The frequency of each feature is plotted alongside each point; the plotted values have been rounded to one decimal place for clarity. The theoretical curves are from (32) with $U = 7.7$ m/s.

the amplitude, and the carrier wave frequency is given by (29), which can be rewritten as

$$2\sigma A_0 = g^2\omega^{-4}(2\gamma)^{\frac{1}{2}}\cosh^{-1}\mathrm{e}^{\frac{1}{2}}. \tag{32}$$

The right-hand side of (32) also depends on U, but this dependence is weak for our parameter regime (10% changes in U or ω yield a 1% change in $\gamma^{\frac{1}{2}}$). Figure 13 is a plot of the observed amplitude A_0 versus the observed width 2σ. The hyperbola are theoretical curves obtained from (32). A weak correlation between the observed ω and the theoretical curves is apparent. Figure 14 is a plot of the observed value of $2\sigma A_0$ versus the theoretical value, which is calculated from (32) using the observed value of ω and $U = 7.7$ m/s. Again, the weak correlation is apparent. (We note in passing that although the six points closest to the ship in figure 14 are above the line, the remaining points do not exhibit a systematic trend with distance aft; we looked for other systematic trends with distance aft and found only a frequency reduction of about 6%.)

We hope that the sinuous fluctuation shown in figure 12 and the variability observed in the data will motivate additional theoretical research. A realistic model for the generation and evolution of the solitary feature is required. Such a model is likely to show that a profile across the feature departs somewhat from the profile of an oblique soliton.

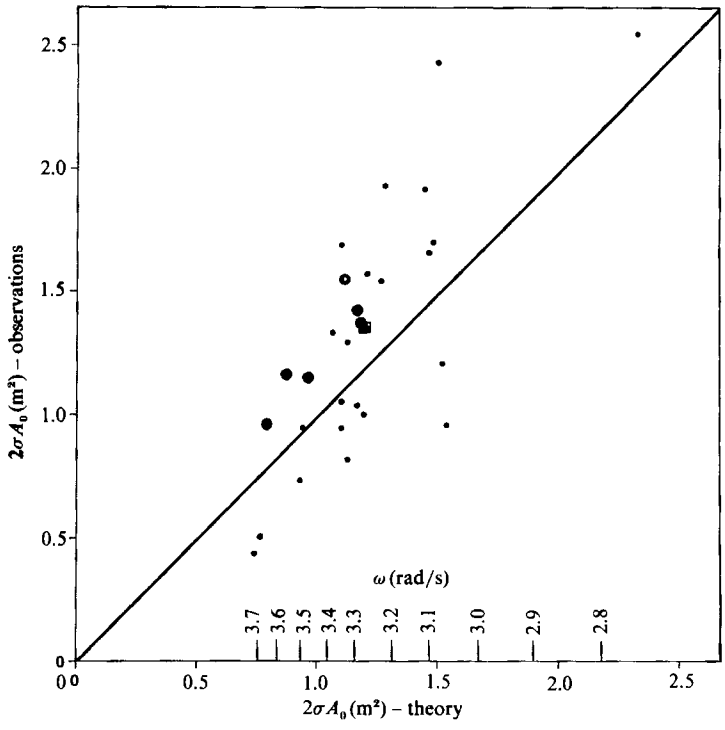

FIGURE 14. Plot of observed value of $2\sigma A_0$ versus theoretical value calculated from (32) using the observed value of ω. Larger points are $\leqslant 0.5$ km aft. The square is the observed average. The two white dots denote overlapping values. The reference line has unit slope.

5 Conclusions

Analysis of thirty data sets of wavestaff measurements of a solitary feature in the Kelvin wake of the Coast Guard cutter *Point Brower* has shown that the average characteristics of the feature between 1 and 4 km aft of the cutter are consistent with those of an oblique nonlinear solitary wave packet. There is considerable variability from run to run, and there is evidence of dispersive spreading before 1 km aft. An aerial photograph shows a sinuous fluctuation of the feature; possible explanations for the fluctuation include small variations in initial conditions or a sinuous instability.

The generation of the feature at the ship remains to be explained. It is not known whether the feature is generated by a fundamentally nonlinear mechanism or by the nonlinear evolution of a diverging wave ray whose initial amplitude could be calculated using one of the linearized Kelvin wave models, such as slender-ship theory (Scragg 1983). In support of the latter mechanism, we note that a linear Kelvin wake generated by a positive point source located at the bow of the cutter and a negative point source at the stern would have an interference maximum at 12.4° in the diverging wave field, which is not far from the observed position of the feature (see Munk *et al.* 1987). Some caution must be exercised in comparing this result to the observed feature because, as noted by C. Scragg (personal communication), a linear ship wave calculation with a realistic hull form may shift the position and structure of the maximum. We also note that the effect of ship motion on the variability of the feature should be examined.

Another important research area is the initial evolution of the feature during the first several hundred metres aft of the ship. As shown in figure 2, the width of the feature is increasing for the first half kilometre, while the change in the width is reduced thereafter. Akylas, Kung & Hall (1988) have studied the nonlinear evolution of a wave packet in which there is a significant increase in the carrier wavelength across the packet. This work, which is applied to a packet in the diverging part of the Kelvin wave field, differs from conventional research where the carrier wavelength is typically assumed to be quasi-uniform or periodic across the domain. The results show that an initial period of linear dispersion can be arrested by nonlinear effects. Calculations for comparison with the present experimental results have not yet been done.

The interaction of the feature with the transverse Kelvin wave and with the ambient wave and current field remains to be examined. In this regard, we note that Cohen *et al.* (1976) and West *et al.* (1987) have shown that plane envelope solitons have limited stability when superimposed upon an ambient wave field.

The solitary feature is a possible explanation for the long bright lines observed in SEASAT SAR images in light to moderate winds. Comparisons between SAR observations and SAR predictions for this type of feature are required to resolve the question. We note that a ray in a linearly diverging Kelvin wave field may also be an explanation for some of the SEASAT lines, but a nonlinear solitary wave packet is a particularly appealing explanation for the longer lines because it does not exhibit linear dispersive decay and therefore remains steeper. Even when it undergoes sinuous fluctuations, it still remains steeper than a linear diverging ray.

Munk *et al.* (1987) analyse sun glitter photos of ship wakes taken from the space shuttle. Some of these photos show several bright lines inside the 19.5° cusp line extending several kilometres aft of the ships. Munk *et al.* (1987) argue that these lines are due to specular scattering from interference rays within a linear diverging Kelvin wave field. Our results suggest that the lines could also be due to nonlinear solitary wave packets. Ironically, Munk *et al.* use one of our aerial photos of the wake of the cutter at 15 knots, taken during the same survey as figures 2 and 12, to illustrate an inner-angle feature.

Finally, we note that ship-generated nonlinear solitary wave packets offer the capability of conducting controlled experiments in the open ocean. For example, observations of the decay of the wave packet in the presence of an ambient wave field can be used to study nonlinear surface wave relaxation processes. In addition, the wave packet can be used to study the interaction of surface waves with fronts.

The success of this experiment was made possible by the efforts of many individuals. Mr William Hicks, Mr Richard Yoder, and Mr Pete Peterson contributed to the design and computer interface of the wavestaff array. The members of the Ballast Point Coast Guard Station spent hours making transects by the ONR Tower. Mr Robert Lawson of ONR coordinated the aircraft overflights from El Toro Marine Corps Air Station. We thank Dr Henry Yuen for references on the sinuous instability. This work was funded under ONR Contract number N00014-86-C-0025.

REFERENCES

Akylas, T. R. 1987 Unsteady and nonlinear effects near cusp lines of the Kelvin ship-wave pattern. *J. Fluid Mech.* **175**, 333–342.

Akylas, T. R., Kung, T.-J. & Hall, R. E. 1988 Nonlinear groups in ship wakes. In *Proc. Seventeenth ONR Symp. Naval Hydrodynamics*. The Hague, Netherlands (to appear).

BRYANT, P. J. 1984 Oblique wave groups in deep water. *J. Fluid Mech.* **146**, 1–20

CHAPMAN, R. B. 1977 Survey of numerical solutions for ship free-surface problems. In *Proc. Second Intl. Conf. on Numerical Ship Hydrodynamics*, pp. 5–16. University of Cal., Berkeley.

CLAUSS, G. F. & BERGMANN, J. 1986 Gaussian wave packets – a new approach to seakeeping tests of ocean structures. *Appl. Ocean Res.* **8**, 190–206.

COHEN, B. I., WATSON, K. M. & WEST, B. J. 1976 Some properties of deep water solitons. *Phys. Fluids* **19**, 345–354.

DOMMERMUTH, D. G. & YUE, D. K. P. 1988 The nonlinear three-dimensional waves generated by a moving surface pressure. In *Proc. Seventeenth ONR Symp. on Naval Hydrodynamics*. The Hague, Netherlands (to appear).

DYSTHE, K. B. 1979 Note on a modification to the nonlinear Schrödinger equation for application to deep water waves. *Proc. R. Soc. Lond.* **A 369**, 105–114.

FLICK, R. E., LOWE, R. L., FREILICH, M. H. & BOYLLS, J. C. 1979 Coastal and laboratory wavestaff system. In *Proceeding of Oceans*, vol. 79, pp. 623–625. IEEE and Marine Tech. Society.

FU, L. & HOLT, B. 1982 SEASAT views oceans and sea ice with synthetic aperture radar. *JPL Publication*, 81–120. Pasadena, CA. 200 pp.

HALL, R. E., LOESER, D. J. & WYATT, D. C. 1987 A model for the short wavelength portion of the surface wave wake of a ship and comparison with observations. *Tech. Rep. SAIC-87/1794.* Science Applications International Corporation, San Diego, CA. 106 pp.

HAMMOND, R. R., BUNTZEN, R. R. & FLOREN, E. E. 1985 Using ship wake patterns to evaluate SAR ocean wave imaging mechanisms. *Tech. Rep. 978*, Naval Oceans Systems Center, San Diego.

HARRIS, F. J. 1978 On the use of windows for harmonic analysis with the discrete Fourier transform. *Proc. IEEE* **66**, 51–83.

HOGBEN, N. 1972 Nonlinear distortion of the Kelvin ship-wave pattern. *J. Fluid Mech.* **55**, 513–528.

HUI, W. H. & HAMILTON J. 1979 Exact solutions of a three-dimensional nonlinear Schrödinger equation applied to gravity waves. *J. Fluid Mech.* **93**, 117–133.

Jane's Fighting Ships. 1985 London: Jane's Publishing Company.

KELVIN, LORD 1887 On ship waves. *Proc. Inst. Mech. Engrs*, pp. 409–434, Plates 80–84. Reprinted in *Popular Lectures*, Vol. III, pp. 450–500, Macmillan.

KERCZEK, C. VON 1975 Numerical solution of naval free-surface hydrodynamics problems. In *Proc. First Intl. Conf. on Numerical Ship Hydrodynamics*, pp. 11–47. David W. Taylor Naval Ship Research and Development Center.

KINSMAN, B. 1974 *Wind Waves.* Dover, 676 pp.

MUNK, W. H., SCULLY-POWER, P. & ZACHARIASEN, F. 1987 Ships from space. *Proc. R. Soc. Lond.* **A 412**, 231–254.

RABINER, L. R. & GOLD, B. 1975 *Theory and Application of Digital Signal Processing.* Prentice-Hall, 762 pp.

SAFFMAN, P. G & YUEN, H. C. 1978 Stability of a plane soliton to infinitesimal two-dimensional perturbations. *Phys. Fluids* **21**, 1450–1451.

SCRAGG, C. A. 1983 A numerical investigation of the Kelvin wake generated by a destroyer hull form. *Rep. SAI-83/1216.* Science Applications International Corporation, San Diego, CA, 46 pp.

SHUM, K. T. & MELVILLE, W. K. 1984 Estimates of the joint statistics of amplitudes and periods of ocean waves using an integral transform technique. *J. Geophys. Res.* **89**, 6467–6476.

STOKER, J. J. 1957 *Water Waves.* Interscience, 567 pp.

WEBSTER, W. C. (ed.) 1986 *Proc. Sixteenth Symposium on Naval Hydrodynamics.* University of California, Berkeley, 613 pp.

WEHAUSEN, J. V. 1973 The wave resistance of ships. *Adv. Appl. Mech.* **13**, 93–244.

WEST, B. J., BRUECKNER, K. A., JANDA, R. S., MILDER, D. M. & MILTON, R. L. 1987 A new numerical method for surface hydrodynamics. *J. Geophys. Res.* **92**, 11803–11824.

WYATT, D. C. & HALL, R. E. 1988 Analysis of ship-generated surface waves using a method based upon the local Fourier transform. *J. Geophys. Res.* **93**, 14133–14164.

YEUNG, R. W. 1982 Numerical methods in free-surface flows. *Ann. Rev. Fluid Mech.* **14**, 395–442.

YUEN, H. C. & LAKE, B. M. 1975 Nonlinear deep water waves: Theory and experiment. *Phys. Fluids* **18**, 956–960.

YUEN, H. C. & LAKE, B. M. 1982 Nonlinear dynamics of deep-water gravity waves. *Adv. App. Mech.* **22**, 67–229.